water

MDPI

Article

A Novel Modular Suspended Underwater Dredging Robot with a Suction and Jet-of-Pump Combination

Xiangsheng Deng [1,2], Jianbin Luo [3,*] and Cuilin Pan [3]

[1] Wuhan Institute of Shipbuilding Technology, Wuhan 430050, China; dengsxwist@163.com
[2] School of Electronic Information and Communications, Huazhong University of Science and Technology, Wuhan 430074, China
[3] GDAS Zhuhai Industrial Technology Research Institute, Zhuhai 519090, China; pancuilin@gdaszh.com
* Correspondence: lk.04@163.com; Tel.: +86-13533963186

Abstract: This article introduces a novel modular suspended underwater dredging robot used for the biochemical reaction tanks of underground water treatment plants. The presented underwater robot can be used to perform dredging operations without touching underwater bottom facilities. The approach achieved a suction and jet-of-pump combination. This requires the underwater robot system to maintain a stable operation attitude in turbulent water flow which is generated by the pump. The study involves the overall design of underwater robots coordinated with the dredging module and details the development of a ground control platform and underwater sensing sonar system. Depending on the location of the dredging, the robot has two operation modes: suspended mode and bottom sitting mode. The experimental results validate the feasibility and effectiveness of the underwater dredging robot. This research can achieve dredging in biochemical reaction tanks without interrupting operations and facilitates the development of intelligent operations in the water treatment industry.

Keywords: biochemical reaction tank; underwater robot; underwater engineering; underwater monitoring; modular; suspended dredging

Citation: Deng, X.; Luo, J.; Pan, C. A Novel Modular Suspended Underwater Dredging Robot with a Suction and Jet-of-Pump Combination. *Water* **2024**, *16*, 3185. https://doi.org/10.3390/w16223185

Academic Editor: Yuan Zheng

Received: 12 October 2024
Revised: 31 October 2024
Accepted: 1 November 2024
Published: 7 November 2024

1. Introduction

With the progression of urbanization, in order to optimize land use and enhance urban landscapes, an increasing number of water treatment facilities are being constructed as underground installations. Statistical data indicate that more than half of the newly built water treatment plants in large cities in China have adopted the underground mode [1]. This presents novel challenges to the operation and maintenance of water treatment facilities.

The cement sand content in urban water treatment plants is generally higher than the designed value, which can lead to equipment abrasion and a shortened service life [2]. The widely used cyclone sedimentation tank is designed to remove sand particles larger than 200 μm, but it is not easy to achieve the design treatment capacity in actual operation. This causes a large amount of fine mud and sand (particle size $\leq$ 200 μm) that can be partially removed in the pretreatment section to enter the subsequent biochemical treatment system, resulting in the serious sedimentation of mud and sand in the biochemical reaction tank (as shown in Figure 1); a low MLVSS/MLSS ratio of sludge, affecting the activity of sludge treatment; an insufficient mixing driving force of mechanical aeration equipment; severe equipment wear; and high operating costs of water treatment plants [3–6]. Therefore, the biochemical reaction tanks of the water-treated plants were regularly dredged.

The traditional method of dredging biochemical reaction tanks requires shutting down water treatment facilities, draining the sewage tank, and requiring personnel to enter the confined space for dredging operations. Based on operational and maintenance experience, dredging work is generally required every 2–3 years, with each shutdown time lasting approximately 15 days in underground water treatment plants.

(**a**) (**b**)

Figure 1. Mud and sand sediments from the biochemical reaction tank.

The disadvantages of traditional dredging methods include not only the negative impact of system disruption on operations but also the high costs and high risks.

Figure 2 illustrates the dangers; this is a confined space operation with difficulties in dissipating toxic gases, leading to high operational risks. The harsher lighting and ventilation conditions in underground water treatment plants make working in biochemical reaction tanks even more hazardous. Thus, it becomes imperative to implement unmanned equipment solutions for dredging operations to mitigate these issues.

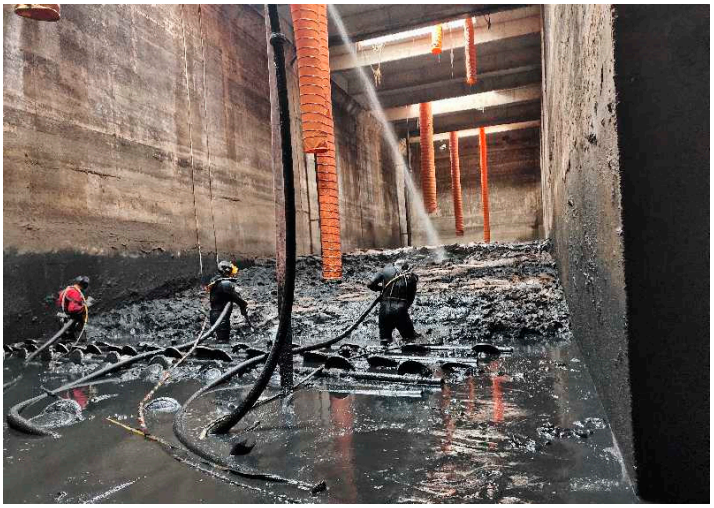

Figure 2. Manual dredging operation of the biochemical reaction tank.

Underwater robots, which are currently widely used, can be classified into two main types: remotely operated vehicles (ROVs) and autonomous underwater vehicles (AUVs) [7].

AUVs are equipped with their own power systems and integrated control systems, allowing them to operate without cable constraints for autonomous navigation and operation. They offer advantages such as extensive operational ranges, deep diving capabilities, and access to intricate structures without needing surface support. However, they have limitations in terms of endurance and payload capacity, so they are typically used for short-range missions involving light loads such as photography, surveying, search operations, and measurement tasks [8–10].

On the other hand, ROVs are connected to operators via umbilical cables, enabling remote control for various underwater activities, including observation, inspection, and construction. The main advantage of ROVs is their ability to transmit power and data

effectively via umbilical cables, allowing them to carry the high-powered heavy equipment required for a wide range of operational needs.

Mai et al. have given an overview of the technical challenges for underwater infrastructure and reviewed and analyzed the current vehicle and instrumentation solutions [11]. In the field of underwater dredging control, an adaptive sliding mode controller combined with a pseudo-inverse-based thruster allocator was designed, which is to address the challenges associated with attitude control and input force allocation for ROV [12]. MPC-based trajectory tracking control for an unmanned underwater tracked bulldozer was developed to improve the stability of trenching and dredging [13]. A new dynamic model for underwater vehicles with a variable mass and center of gravity in underwater dredging missions was proposed for a theoretical basis [14]. Zhang et al. designed an underwater dredging robot with two modes to clean deep cave walls. The underwater dredging robot could effectively clean the adsorbed Limnoperna fortune in long-distance water conveyance tunnels [15]. Arykantsev et al. described an underwater walking robotic mini dredger with higher capabilities for ground and profile cross-country ability. To determine the carrying capacity, the task of loading the frame of the walking device was solved [16]. Li et al. analyzed the desilting efficiency of the spiral dredging auger, according to the characteristics of underwater desilting, through analysis and theoretical calculation, providing a better design of a spiral silting stranding dragon [17]. Shademani et al. presented a robotic system for removing weeds and sediments in the existing irrigation systems, with less damage to the canals [18]. Yang et al. reviewed the designs and performance of different adsorption methods for underwater robots and presented effective visual observation, control, and autonomous technologies [19]. Regarding the research of underwater lift pumps, Ji et al. reviewed the research progress of pumps in deep-sea resource exploitation and offered theoretical and engineering support for the development of underwater mining slurry pumps [20].

Crawler underwater dredging robots have been widely used to clean sludge in sewage tanks, as shown in Figure 3, but the equipment cannot be applied in environments with facilities at the bottom of the tank. Owing to the design of the biochemical reaction tank in the underground water treatment plant, when dredging above the aeration section (as shown in Figure 4), the underwater robot must maintain a certain distance from the bottom of the tank to avoid contact with and damage to the aeration facilities.

Figure 3. Crawler underwater dredging robot operation of the sewage tank.

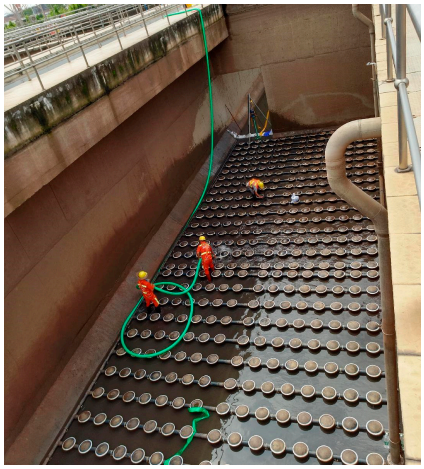

Figure 4. Manual dredging operation of the aeration section.

2. Materials and Methods

2.1. Design

According to the configuration of the biochemical reaction tank of the underground water purification plant, the maximum water depth during operation is not more than 15 m, the area of a single corridor is approximately 1200 m^2, the working space of the underwater dredging robot is approximately 18,000 m^3, and the working range is not more than 50 m from the launching point of the robot.

Specifically, the practical use of underwater dredging robots in the biochemical reaction tanks of underground water treatment plants presents several key requirements:

1. Capable of suspended dredging without touching the bottom facilities during operation.
2. Capable of carrying sufficient operational loads.
3. Capable of achieving multiple degrees of freedom in movements, including floating, diving, advancing, retreating, turning, and rolling in water. Additionally, it must be able to perform fixed depth, navigation, and rolling actions.
4. Ability to operate in zero-visibility sewage.
5. Cost-effective control and maintenance.
6. Easy operation and maintenance.

2.2. Operation Mode

For the dredging of non-aerated sections, underwater robots can use a bottom sitting method to clean the deposited sediment and improve operational efficiency [21–23]. Hence, the operation modes can be divided into the following:

1. Water surface mode: The robot partially protrudes from the water surface, allowing the operator to visually locate the position of the robot. When necessary, the robot will sink. This mode is commonly used for detection and movement, where robots are equipped with overhead multibeam or side-scan sonar to scan underwater surfaces and can only dive after discovering targets or determining work points.
2. Suspended mode: The robot is suspended in the water. By turning on the fixed depth mode, the robot can always keep diving to a certain depth underwater or maintain a certain height with the bottom of the water. This mode requires the robot to be completely immersed in the water and never touch the bottom of the water. It can perform corresponding operations in a fixed state, such as underwater jetting, etc., as shown in Figure 5.
3. Bottom-sitting mode: The robot dives to the bottom of the water and moves on a plane with the bottom of the water [24,25]. The bottom of the robot comes into contact with the mud at the bottom of the water column, generating friction and improving the stability of the robot. It can also maintain a fixed posture in the water flow [26–29].

This mode is used for robot underwater dredging at the section of the sewage tank without any bottom device, such as anaerobic and anoxic sections, referred to as the non-aeration section subsequently, as shown in Figure 6.

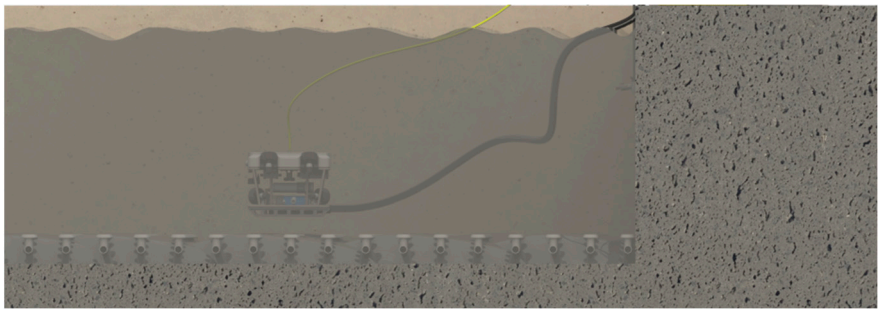

Figure 5. Suspended dredging operation of the aeration section.

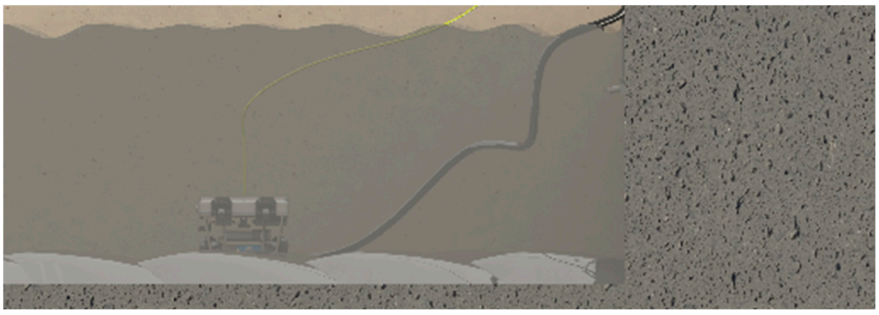

Figure 6. The bottom-sitting dredging operation of the non-aeration section.

The underwater dredging robot system comprises an ROV, a ground control platform, power distribution equipment, a dredging module, and underwater sensing sonar. The system composition is depicted in Figure 7.

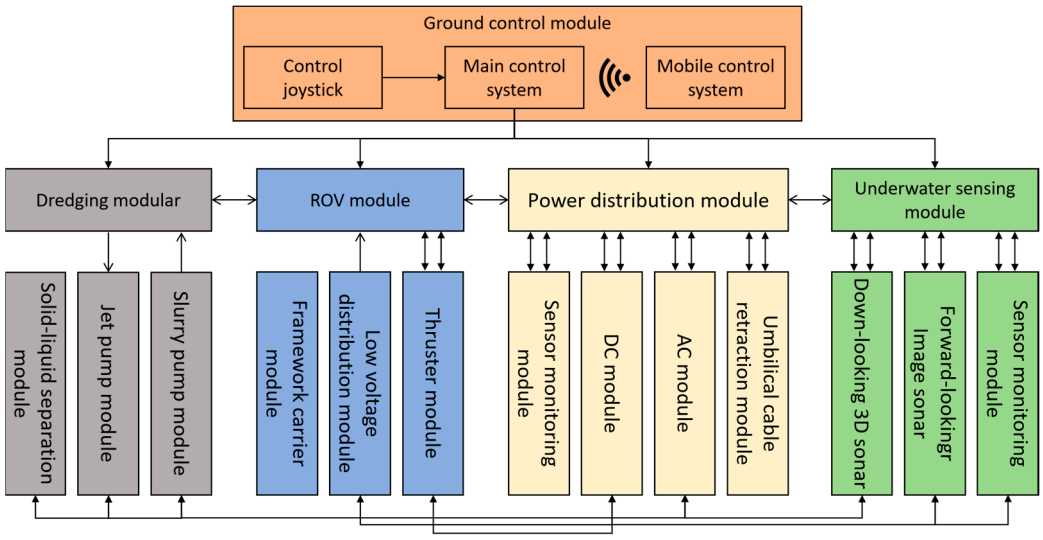

Figure 7. Composition of the underwater robot modules.

The ROV uses multiaxis vector propulsion technology in the propulsion module to improve the maneuverability and stability of the underwater robot, especially during low-speed navigation. This enables more flexible and accurate positioning and movement underwater. The ground control platform and power distribution equipment were set on the ground to supply power and transmit signals to the ROV through a composite umbilical cable [30].

The underwater sensing module integrates advanced sensors such as distance sensors, depth sensors, attitude sensors, and sonar into the navigation and depth determination systems of the ROV. These sensors provide accurate environmental data and robot status information, helping the system perform better self-adjustment. In underwater environments, the ROV adopts new communication technologies of optical communication to ensure a stable connection with operators or other devices due to the limitations of traditional wireless wave propagation.

2.3. ROV Module

The ROV has a modular design, allowing for the quick replacement or upgrading of different components of navigation and depth determination systems to meet specific task requirements [31].

The modular design of the ROV follows a sandwich structure, which can be divided into upper-level, middle-level, and lower-level modules. The upper module includes an expandable modular buoyancy body, an umbilical cable connector, and a release and recovery device. The middle module includes a vertical thruster, functional service cabin, horizontal thruster, main framework, and reserve space for the dredging module at the center position of the main framework. The lower module includes sliding shoes, adjustable buoyancy configuration space, and a dredging module. The ROV module composition is shown in Figure 8.

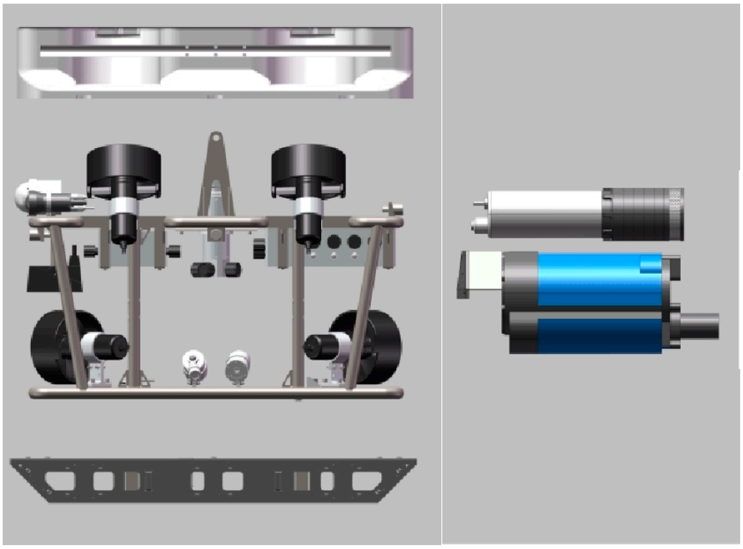

Figure 8. Sandwich structure and dredging module of the underwater robots.

The ROV consists of a framework, a buoyancy body, and a sliding shoe mechanism. The framework includes a top frame for supporting the buoyancy bodies and a bottom frame for installing sliding shoe mechanisms. These frames are connected by connecting rods.

The proposed configuration enhances the ease of adjusting the weight of underwater robots and improves their adaptability to various underwater environments, thereby increasing the lifting efficiency of these robots. A 3D simulation illustrating the operation of the ROV is presented in Figure 9.

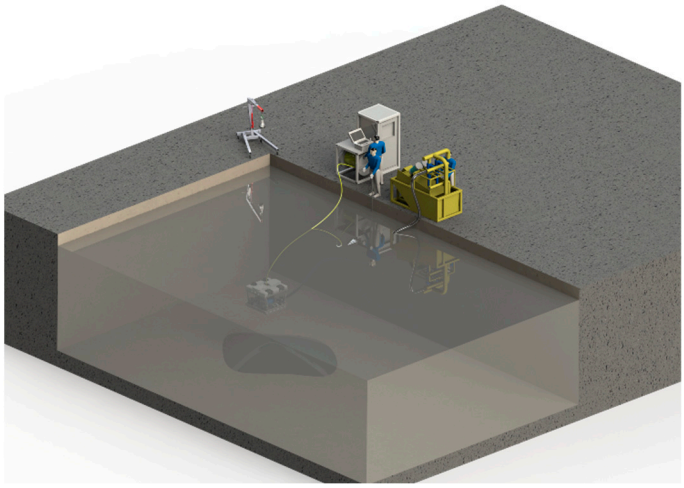

Figure 9. 3D simulation of underwater dredging robot operation.

2.3.1. Thruster and the Thrust Calculation

The thruster uses magnetic coupling transmission technology to ensure zero leakage without dynamic sealing requirements, which eliminates the dependency on external pressure compensators. The 3D design of the thruster structure is depicted in Figure 10.

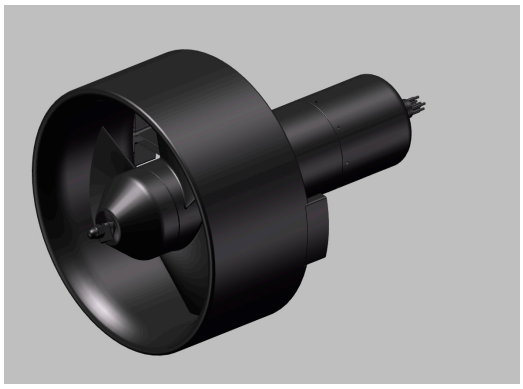

Figure 10. 3D structure of the thruster.

Each thruster generates a thrust capacity reaching up to 32 kg both forwards and backwards, encasing an aluminum alloy shell weighing approximately 5.3 kg in air versus only approximately 3.8 kg when submerged—the angle formed between each robot's forwards-facing direction and the respective horizontal thrust vector is measured precisely at 45°. With individual thrust values set at approximately 30 kg leading towards diagonal force contributions totaling approximately 210 N combined, an aggregate output nearing 840 N across all four units collectively engaged throughout operations conducted beneath water surfaces [32,33].

After calculation and analysis, the anti-flow area on the front of the robot is 0.5 m^2. When the robot travels against the water, the water resistance is at a maximum, and the resistance required to flow is at a maximum. At this time, the relative flow velocity of the water flow is at a maximum, according to the water resistance formula:

$$F = \frac{1}{2} C \rho_W (V_R + V_W)^2 S_f \quad (1)$$

where C is the resistance coefficient with the value 2, ρ_W is the water density, V_R is the ROV velocity, and V_W is the Water flow velocity; the calculation of the static and moving water resistance of the robots under different flow velocities is shown in Table 1.

Table 1. Calculation table for the required thrust under different equivalent water velocities.

Equivalent Water Velocity	1.5 Knots	2 Knots	2.5 Knots	3 Knots
	0.77 m/s	1.03 m/s	1.28 m/s	1.54 m/s
Longitudinal water resistance N	296	314	515	1222
Lateral water resistance N	385	408	669	1588

In addition to the water resistance of the ROV, it also needs to overcome the drag force of umbilical cables and slurry hoses.

According to the drag force formula:

$$F_d = \frac{1}{2} S A V^2 C_d \tag{2}$$

where S is the value of water density/gravity acceleration, A is the cable diameter in inches divided by 12 times and multiplied by the length of the cable perpendicular to the flow, V is the velocity, and C_d is the drag force coefficient without any vector. The drag force of different velocities is shown in Table 2.

Table 2. Calculation table for the required thrust of different distances.

Velocity	1.5 Knots	2 Knots	2.5 Knots	3 Knots
	0.77 m/s	1.03 m/s	1.28 m/s	1.54 m/s
20 m	96	171	267	385
30 m	144	257	401	578
50 m	240	428	668	963

The aquatic maneuverability of ROVs can subsequently be derived via established design parameters alongside specific performance metrics associated directly with those same aforementioned propulsion systems [34–39].

To ensure optimal mobility for underwater robots, eight thrusters are integrated into their design—four vertical thrusters paired with four horizontal thrusters. Each vertical sensor is installed at a 20° angle. This arrangement provides both vertical thrust (upwards or downwards) and lateral thrust during vertical maneuvers to maintain stability while enhancing sensitivity during roll movements [40,41].

The four horizontal thrusters positioned at 45° enable multidirectional horizontal movement through coordinated speed adjustments while granting turning capabilities to the robot, as shown in Figure 11.

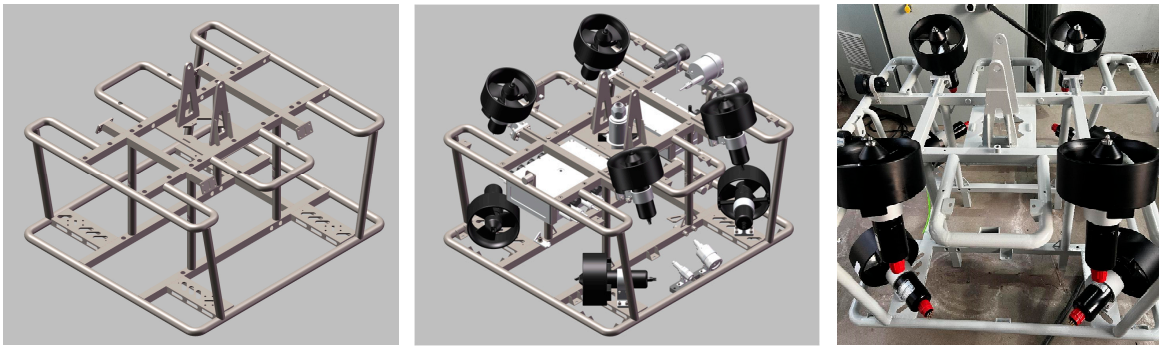

(**a**) (**b**) (**c**)

Figure 11. 3D structure of the main framework: (**a**) metal main frame; (**b**) installation of thrusters, watertight compartments, light sources, cameras, fiber optic transceivers, and electrical joints on the main frame; (**c**) actual installation of the main framework.

2.3.2. Main Framework

Characterized by versatility, the ROV features an open frame structure that allows for the straightforward installation, adjustment, replacement, and maintenance of its diverse modules and instruments. The ontology framework serves as a primary connector within this sandwich structure; it supports and protects critical components such as pressure-resistant electronic cabins, thrusters, detection tools, and operational implements, as illustrated in Figure 11.

When both appearance and structural integrity are designed for this ontology framework, the following considerations must be given [42]:

1. Low hydrodynamic resistance coupled with excellent navigational performance.
2. Adequate strength specifications.
3. Simplified arrangement options for component mounting.
4. Superior processing capabilities.

Commonly utilized materials such as aluminum alloy or stainless steel should align with strength requirements while aiming to minimize the overall structural weight; thus, it is recommended that a six-series aluminum alloy be employed owing to its high strength-to-weight ratio along with its corrosion resistance properties—other auxiliary components should ideally utilize aluminum from similar series or stainless steel where feasible.

The framework will incorporate single-point lifting mechanisms at its apex alongside convenient attachment points located at its front end designed specifically for carrying detection equipment or lighting apparatuses effectively—a robust full-width crash barrier featuring D-shaped rubber strips can significantly mitigate impact forces resulting from collisions; rounded corner protections should also be incorporated across all types of equipment, including frame materials.

2.3.3. Buoyancy Body and Skateboard

The buoyancy body is streamlined to minimize water resistance and flow disturbance and can be assembled using different volume buoyancy body modules, which are processed via CNC to form various desired configurations [43,44], as shown in Figure 12.

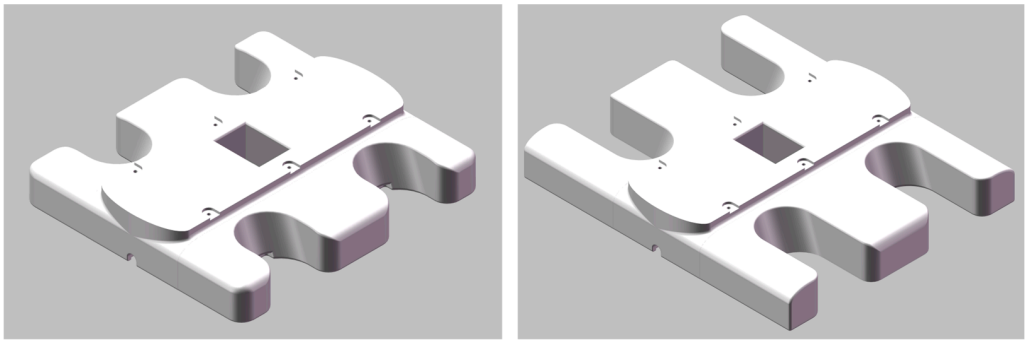

(**a**) (**b**)

Figure 12. 3D structure of the buoyancy body: (**a**) standard type and (**b**) enlarged type.

The standard-type buoyancy body is capable of furnishing a variable load of approximately 120 kg for the ROV, which can be modulated through a ballast (such as lead blocks) strategically arrayed around the system. When a replaceable dredging module is installed, the ballast can be removed, enabling the ROV to maintain a state of positive buoyancy or gravity during operational processes in accordance with specific operational mode requirements.

The material selection for the buoyancy body is pivotal for ensuring both reliability and safety in ROV operations. It must withstand sewage pressure while demonstrating minimal density, low water absorption rates, and superior mechanical processing capabilities.

The buoyancy material comprises composite foam plastic that is cast into an epoxy resin shell using closed microspheres. To safeguard this buoyancy material from potential collisions during operation, the application of a high-strength protective film primarily composed of polyurethane on its outer surface is needed. The performance parameters for various buoyancy materials are detailed in Table 3.

Table 3. Performance parameters of different labelled buoyancy materials.

Different Buoyancy Material Labels	Density (g/cm^3)	Hydrostatic Strength (MPa)	Water Absorption Rate (%)
0375	0.375 ± 0.010	≥6	≤1
0385	0.390 ± 0.010	≥8	≤1
0395	0.400 ± 0.010	≥10	≤1
0415	0.420 ± 0.010	≥15	≤1
0450	0.450 ± 0.010	≥24	≤1
0510	0.520 ± 0.010	≥40	≤1

To facilitate smooth movement over underwater sediment via thrusters during operations, a bottom skateboard structure has been devised. This skateboard is fabricated from high-strength composite materials that endure underwater pressure and possess favorable mechanical properties. The underside of a skateboard must exhibit outstanding wear resistance when interacting with underwater sediment [29], as illustrated in Figure 13.

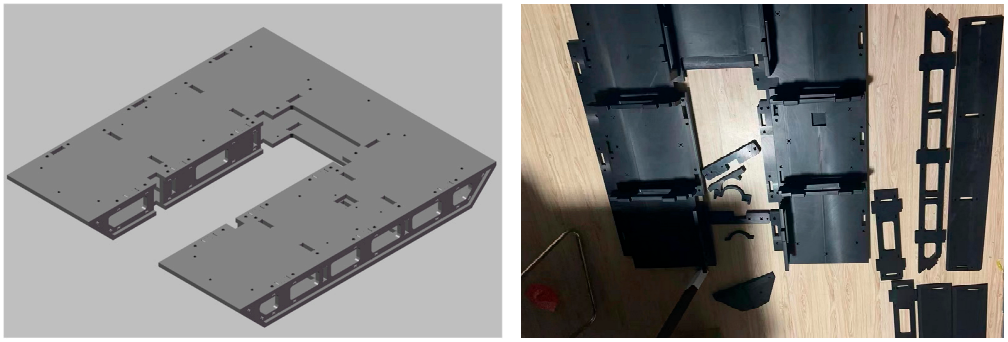

(**a**) (**b**)

Figure 13. Underwater skateboard: (**a**) 3D structure; (**b**) Installation.

The internal architecture of the skateboard features a hollow configuration that creates an array of cubic spaces capable of accommodating buoyancy blocks and ballasts with varying densities, as needed. This arrangement allows adjustments to be made regarding buoyancy, gravity, and center-of-mass positioning. By establishing grids for buoyancy and gravity on the *yz* plane, adjustments can be made to optimize the robot's overall center of gravity position, as illustrated in Figure 14.

There are several ways to modify the skateboard space:

1. Keeping the interior empty and filling it with water during underwater operations.
2. Installing a larger modular buoyancy body to achieve positive buoyancy.

$$f_B = V_F(\rho_W - \rho_B)g \quad (3)$$

where V_F is the space volume that fills the block, ρ_W is the water density, ρ_B is the buoyancy block density, and g is gravity. The positive buoyancy interval range is 188.2–245 N.

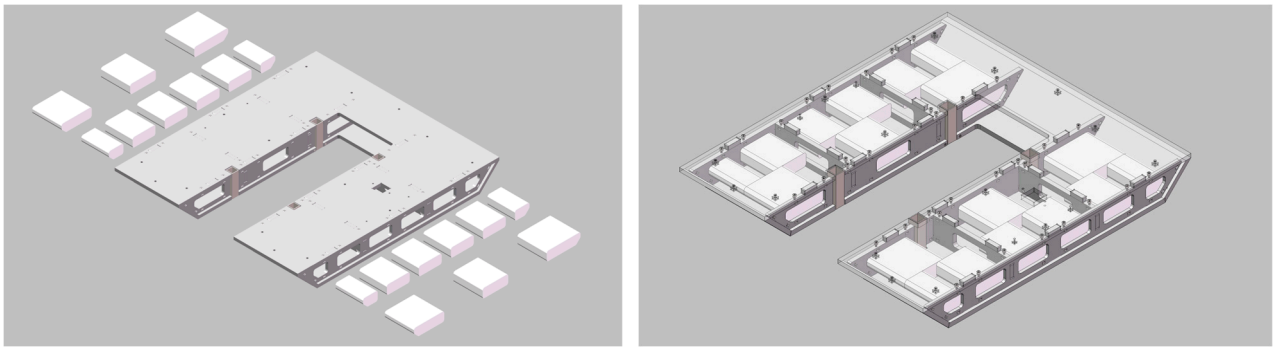

(**a**) (**b**)

Figure 14. Underwater skateboard with a barycentre adjustment block: (**a**) buoyancy and ballast block; (**b**) buoyancy or ballast block installed on the skateboard.

Installing inflatable airbags (considering the water pressure bearing capacity of the airbags, they can be used only in shallow water, and the dredging depth of the biochemical reaction tank in underground water treatment plants generally does not exceed 15 m) provides

$$f_{\mathrm{B}} = V_{\mathrm{I}}\rho_{\mathrm{W}}\mathrm{g} \tag{4}$$

where V_{I} is the volume of the interior space of the skateboard, ρ_{W} is the water density, and g is gravity. The positive buoyancy interval range is 490 N.

Installing zinc blocks for seeding provides

$$f_{\mathrm{B}} = V_{\mathrm{F}}(\rho_{\mathrm{Z}} - \rho_{\mathrm{W}})\mathrm{g} \tag{5}$$

where V_{F} is the space volume that fills the block, ρ_{Z} is the ballast zinc block density, ρ_{W} is the water density, and g is gravity.

The underwater buoyancy of the ROV in this study can be adjusted within the range of −384.86 to 490 N, facilitating operation across diverse underwater modalities. Variations in buoyancy among different modules may result in shifts in the robot's overall center-of-mass, necessitating appropriate adjustments; achieving equilibrium involves configuring adjustable modules accordingly—this balance plays a vital role across various underwater tasks by allowing manipulation at differing angles of elevation and depression.

The ROV experiences the influences of both gravitational forces and buoyant forces while navigating submerged environments; these interactions can be articulated through an established formula

$$P + B = \begin{pmatrix} -(P-B)\sin\theta \\ 0 \\ (P-B)\cos\theta \\ -(z_G P - z_B B)\sin\theta - (x_G P - x_B B)\cos\theta \\ (y_G P - y_B B)\sin\theta \end{pmatrix} \tag{6}$$

In this equation, P represents the gravitational force, whereas B denotes the buoyant force acting upon the robotic entity. x_G, y_G, and z_G correspondingly denote coordinates related to its center of gravity, whereas x_B, y_B, and z_B pertain similarly but focus on centers associated specifically with buoyancy dynamics. Owing to the installation of buoyancy blocks on the underwater dredging robot body, buoyancy and gravity are approximately two forces of equal magnitude during movement. The center of gravity of the underwater

dredging robot is at the origin position in the body coordinate system, with $x_B = y_B = 0$ in the center of buoyancy coordinates. The formula can be simplified as follows:

$$P + B = \begin{pmatrix} 0 \\ 0 \\ 0 \\ mg \cdot z_B \cdot \sin\theta 0 \\ 0 \end{pmatrix} \tag{7}$$

The equation shows that gravity and buoyancy counteract each other in the longitudinal, lateral, vertical, and rotational motion of the ROV and affect only the longitudinal tilt motion.

When individual components comprising this particular model are assembled, the accurate calculation of the positions corresponding to the respective centers concerning both mass distributions along the chosen coordinate systems becomes imperative. Notably, the location attributed to the buoyancy central point representing the totality should remain elevated above those indicating the center of gravity.

To ensure an optimal working posture coupled with stability while operating beneath water surfaces, the stable height achieved by such robots should exceed the minimum threshold, thereby permitting timely corrective measures based on the restoring torque exerted throughout motion sequences to maintain the desired levels of steadiness.

The specific calculation methodologies employed to ascertain the relationships governing the overall distributions related to the aforementioned concepts yield the following results:

$$\frac{X_g = \frac{\sum M_x}{\sum W}, Y_g = \frac{\sum M_y}{\sum W}, Z_g = \frac{\sum M_z}{\sum W}}{X_c = \frac{\sum M\prime_x}{\sum W}, Y_c = \frac{\sum M\prime_y}{\sum W}, Z_c = \frac{\sum M\prime_z}{\sum W}} \tag{8}$$

Efforts directed towards sustaining the stable heights denoted as h aligning vertically against the coordinates indicative of the respective centers yield the relationship expressed mathematically, where $h = Z_c - Z_g$. Through adjusting the framework, spatial arrangements, and inherent characteristics among the constituent elements, noncompliant designs are rectified, ultimately resulting in the following relationship between the center of gravity and the center of buoyancy:

$$\tan\varphi_0 = \frac{X_c - X_g}{Z_c - Z_g} \tag{9}$$

In accordance with the stipulated standards for the requisite stability observed in underwater robots, the dimensions φ_0 should be maintained strictly within the confines ranging from 0° and 3°. The structural layouts encompassing all module aspects incorporated therein subsequently require fine-tuning to ensure that compliance with the requisite conditions is met satisfactorily.

2.3.4. Parameters

As the carrier for underwater dredging operations, the size parameters and other information of the ROV are shown in Table 4.

Table 4. Calculation table for the required thrust under different equivalent water velocities.

Parameters	Value
Dimensions	≤1200 mm × 1100 mm × 1000 mm
Weight (with payload)	300 kg
Max payload	120 kg
Total buoyancy	2615–3490 N
Water depth	100 m

Table 4. *Cont.*

Parameters	Value
Operating speed	0–2.5 knot
Number of thrusters	8
Arrangement of thrusters	4 × Horizontal 4 × Vertical
Type of thrusters	Magnetic coupling
DOF	6

The 3D structure of the underwater dredging robot is presented in Figure 15.

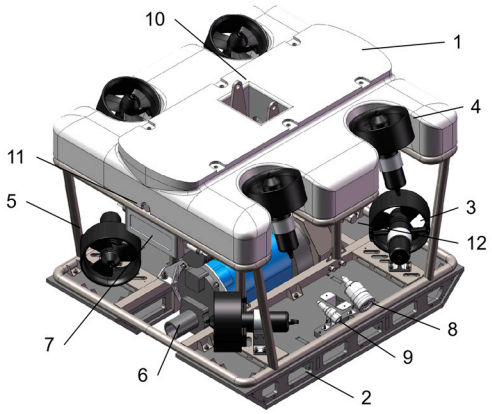

Figure 15. In the figure, 1—buoyancy body, 2—skateboard, 3—horizontal thruster, 4—vertical thruster, 5—main framework, 6—dredging module, 7—watertight compartment, 8—searchlight, 9—camera, 10—lifting module, 11—forward sonar, 12—side sonar. 3D structure of the underwater dredging robot.

2.4. Ground Control Platform Design

A kinematic and propulsion system model for an ROV is established using its mechanical parameters [45–47]. The motion controller calculates the required forces and torques for each degree of freedom based on commands from an upper computer along with current state feedback before these forces and torques are distributed to corresponding thrusters via a thrust distribution algorithm, thereby achieving effective motion control over the underwater robot. The control design is illustrated in Figure 16.

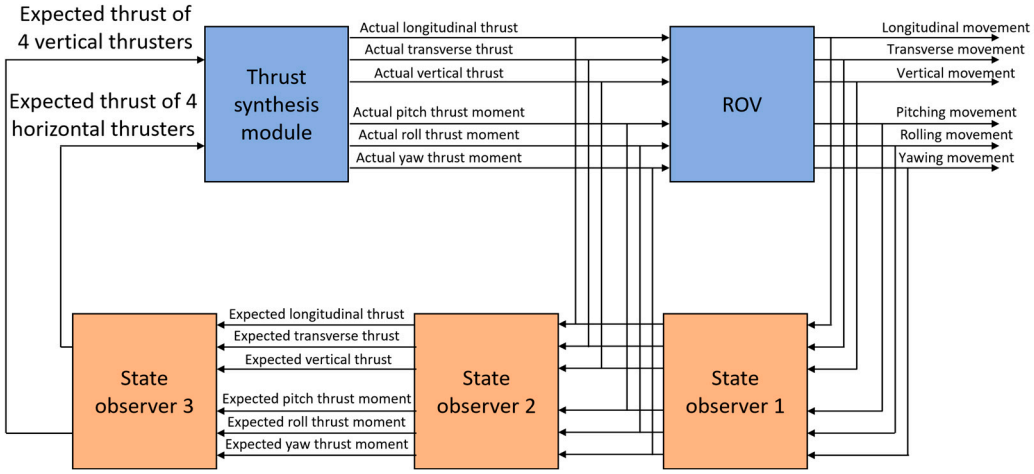

Figure 16. Thrust distribution control design.

The ROV can be maneuvered across six degrees of freedom by receiving directives from an upper computer that governs its movements while calculating the thrust magnitude and direction necessary to propel it effectively [48]. During operation, external factors such as water flow may influence performance; thus, sensors provide critical feedback regarding ROV motion data, which informs Proportional Integral Derivative (PID) algorithms used to regulate robotic attitude control continuously within a loop until objectives are met [49]. The process is further detailed in Figure 17.

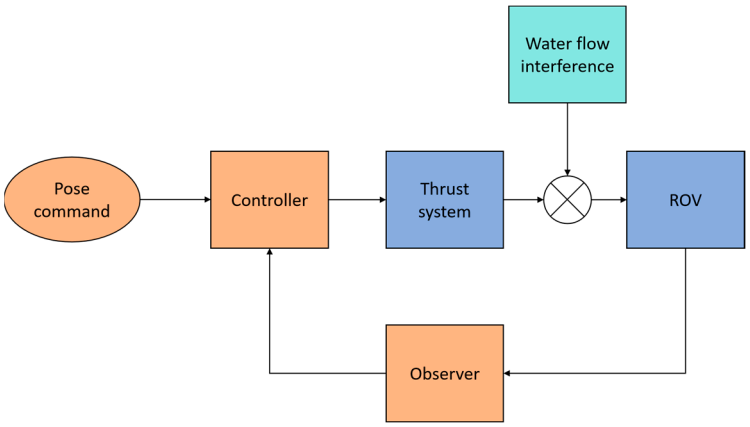

Figure 17. PID control feedback process.

For the suspended dredging mode, the most important depth control function is the key to ensuring that the ROV does not touch the facilities at the bottom of the biochemical reaction tank. Two types of depth sensors, depth gauge and bathymetry sonar, were used for depth control, as illustrated in Figure 18.

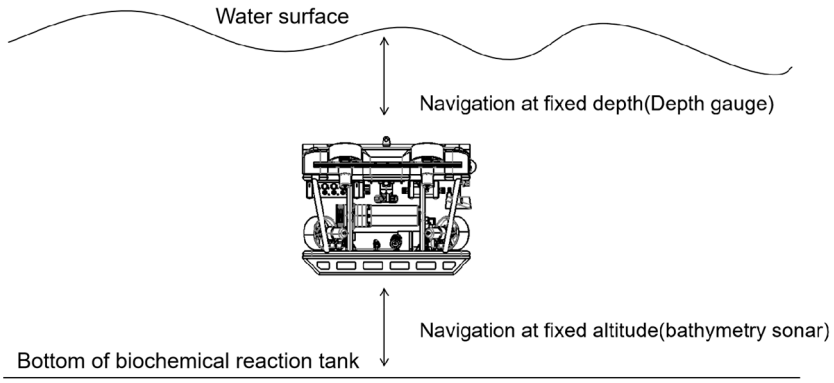

Figure 18. Two modes of suspend control.

Through PID algorithms, combined with data from depth sensors, attitude sensors, and electronic compasses, the ROV can achieve depth control, directional control, and cruise control modes. The control interface representations are shown in Figure 19.

Communication between control consoles and the ROV employs fiber optics transmission, whereby transmitted signals reach fiber optic transceivers onboard before entering into local area networks facilitated by switches connecting all devices functioning collectively as network nodes, allowing for independent remote access/management capabilities per device.

For industrial bus devices, signal conversion involves seamlessly transforming industrial bus signals into Ethernet signals.

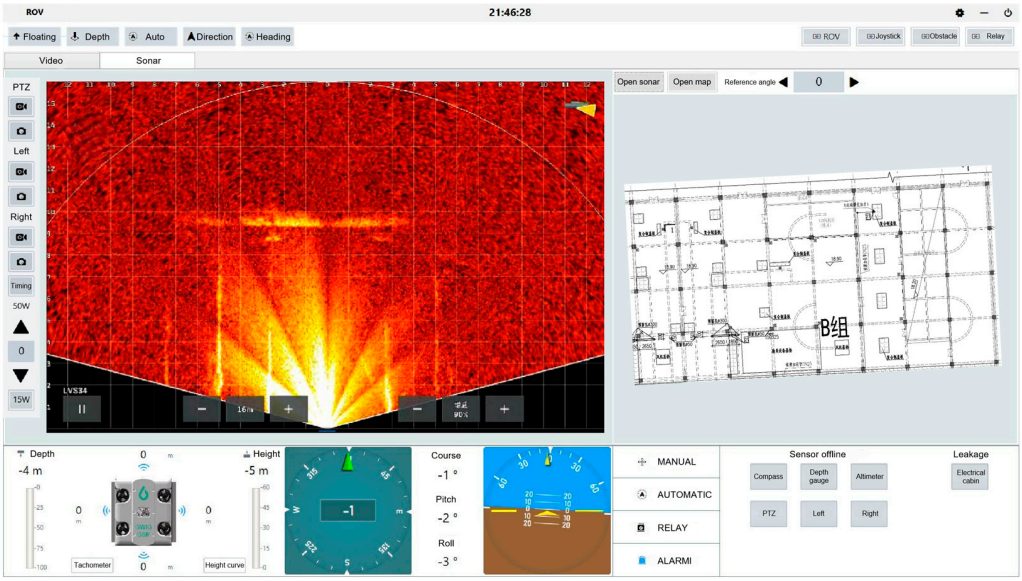

Figure 19. Control interface.

2.5. Power Distribution Design

The primary function of the power cabinet is to continuously supply DC/AC power to the ROV and the dredging module. Since the power of the ROV exceeds 20 kW, and considering the power loss of the umbilical cable, the output power of the surface power source must be sufficiently large [50,51]. The power supply of the power cabinet is AC 380 V, and it outputs a stable 600 V DC power supply for the underwater thruster through the rectifier. Additionally, it provides a 380/220 V AC power supply for the submersible slurry pump and the underwater jet pump, and the low-voltage part of the control and sensing system is supplied with 220 V to 48/24/5 V DC. The 220 V AC power supply also serves as the output interface to provide power transmission for the water surface control panel. The electrical connection design is illustrated in Figure 20.

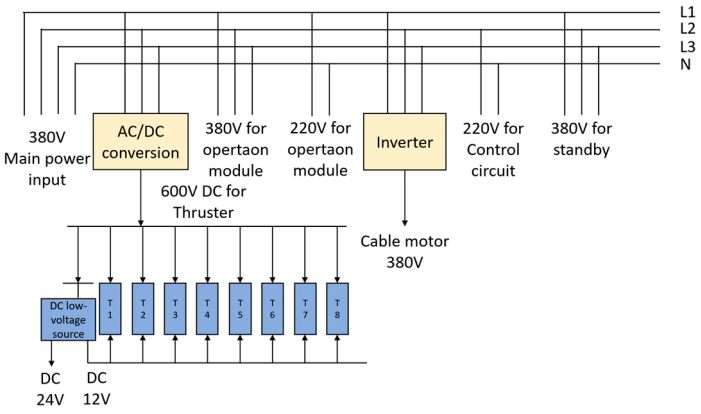

Figure 20. Electrical connection design.

2.6. Dredging Module

The dredging module is the main operational module of the underwater dredging robot system, which includes an underwater slurry pump for extracting sediment from the bottom of the biochemical reaction tank, an underwater jet pump for flushing sediment from the bottom of the water column [52,53], and solid–liquid separation equipment on the ground. The overall structure of the ROV is engineered around these slurry pumps and jet pumps.

Sufficient suction capability must be ensured through adequate power provision for the slurry pump. Due to underwater mud and sand sediment deposition, the additional installation of a jet pump facilitates flushing actions, lifting sediments trapped within gaps around aeration devices.

The coordination of both pumps increases the sand pumping efficiency of the dredging module. The extracted slurry mixtures are transported upwards via slurry hoses undergoing solid–liquid separation processes at separators where filtered wastewater is refluxed into biochemical reaction tanks [54]. The combination of dredging modules is shown in Figure 21.

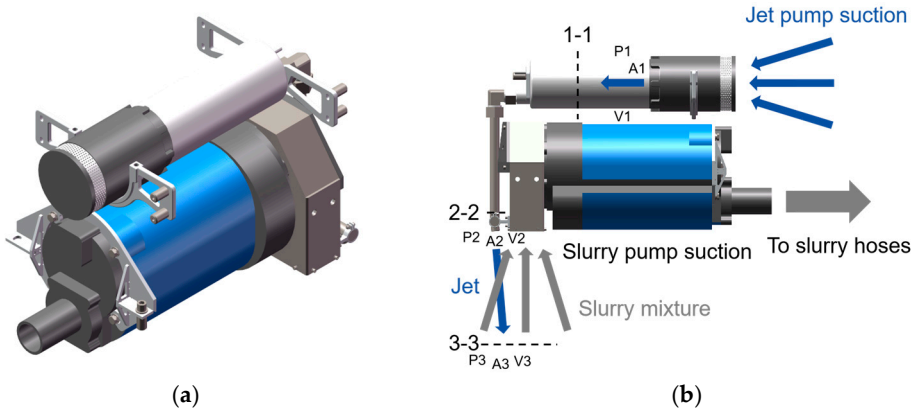

Figure 21. The combination of dredging modules: (**a**) 3D structure of the dredging module; (**b**) fluid direction of the dredging module.

After being pressurized by a high-pressure pump, the water is transported along the pipeline to the jet nozzle, where it forms a water jet after being sprayed out. A1 is the cross-sectional area inside the high-pressure pipe, with a diameter of d1 = 20 mm inside the pipe; P1 is a pressure range of 1-1 with a magnitude of 0.5 MPa; and the flow rate of the jet pump is 4 m^3/h.

According to the flow formula, input the relevant parameters into the Bernoulli equation to obtain

$$\frac{P_1}{\gamma} - \frac{P_2}{\gamma} = \frac{V_2^2}{2g} - \frac{V_1^2}{2g} \tag{10}$$

According to the calculation, the jet velocity at the nozzle outlet position is 31.42 m/s.

The sediment entering the water treatment plant is predominantly introduced by rainfall runoff, which constitutes more than 90% of the total sediment load. On clear days, fine particles with a diameter of less than 200 μm account for 98.3% of the sediment; during peak rainfall events, this proportion decreases to 71.6%. The filter screen designed for separating mud from water has a mesh size of 300 and a pore diameter of 48 μm, effectively isolating most sediment particles within the biochemical reaction tank. However, owing to its low permeability, it requires pressurized filtration to facilitate water passage [55–57].

2.7. Underwater Sensing Sonar Design

In underwater sewage environments characterized by zero visibility, traditional underwater cameras and searchlights are ineffective in gathering environmental information. Consequently, sonar imaging has emerged as the only viable solution under current technological constraints. Fortunately, underground water treatment facilities typically possess detailed design schematics that can be integrated with sonar imagery to serve as reference points for ROV positioning [58].

The front section of the robot is equipped with forwards sonar technology to monitor underwater sewage environments and detect obstacles ahead, as illustrated in Figure 22.

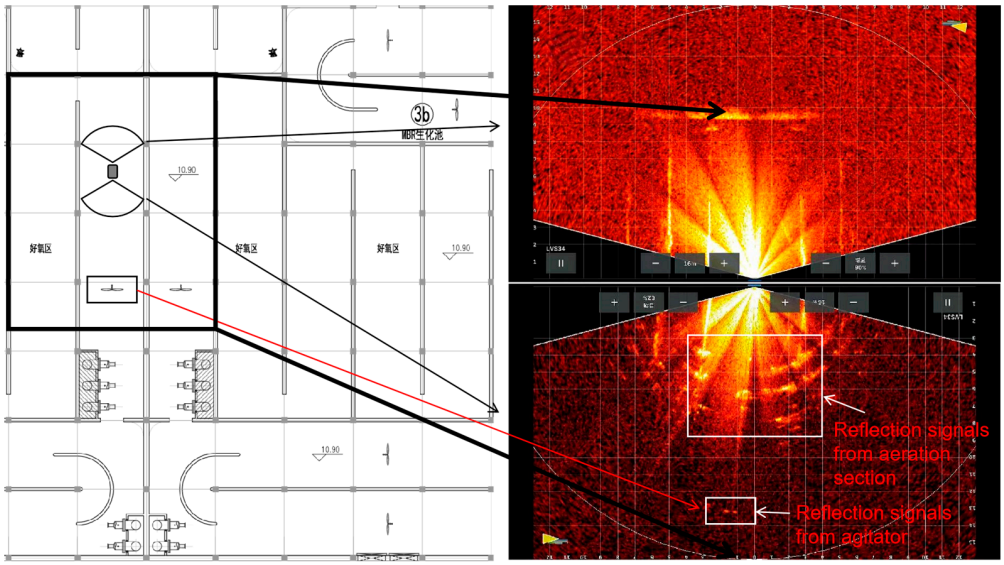

Figure 22. Forwards-viewing sonar imaging (comparison with the drawing of the biochemical reaction tank in the underground water treatment plant).

Additionally, a downwards-viewing sonar positioned near the water surface aids in robot localization within underwater sewage environments—a critical feature given the complexities inherent in such settings. The underwater dredging robot system employs multibeam detection technology alongside 3D sonar image scanning techniques to generate comprehensive 3D representations of target objects and evaluate the thickness of underwater sediment in the biochemical reaction tank.

Both methodologies leverage acoustic principles for conducting underwater mapping through sound wave emission and reception directed towards the seabed. Furthermore, a fixed-point downwards-viewing sonar system, as shown in Figure 23, is installed adjacent to the water surface to create 3D point clouds representing both submerged environments and robotic positions [59]. For monitoring activities within confined aquatic areas, the use of fixed-point downwards-viewing sonars dedicated solely to target surveillance tasks is proposed. These devices are firmly mounted on rigid structures beside the sewage tank, thus avoiding the complications related to compensating for wave-induced vibrations, greatly simplifying equipment complexity and reducing overall costs.

By integrating both downwards-viewing sonar and forwards-viewing sonar, operators can control ROV effectively from both third-person and first-person perspectives.

The ROV can be equipped with underwater acoustic corner reflectors designed specifically to distinguish its body from surrounding objects within underwater sewage environments. These reflectors produce strong reflection signals that facilitate rapid location identification via imaging techniques.

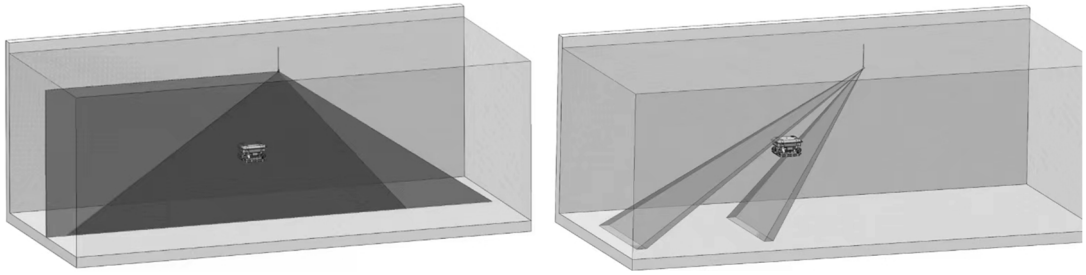

(**a**) (**b**)

Figure 23. *Cont.*

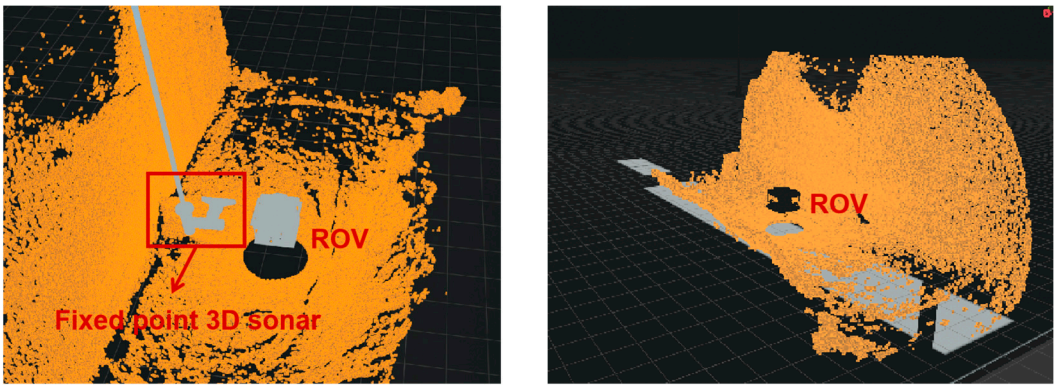

(**c**) (**d**)

Figure 23. Fixed-point 3D sonar installed near the water surface: (**a**) panoramic scanning mode; (**b**) downward scanning mode; (**c**) fixed-point 3D modeling and the relative position of ROV; (**d**) downwards-viewing 3D point cloud sonar image.

2.8. Digital Twins for Operation Scenarios

Given the poor visibility conditions prevalent in sewage contexts, visual observation or operation using optical equipment submerged in underwater sewage environments is precluded. An advanced virtual reality digital twin system was established, which has the ability to recreate complex details of both aquatic environments and robotic movements by means of sophisticated 3D graphics rendering processes.

This innovative approach operates by capturing signals pertaining to directly related posture states emitted by the robots themselves while simultaneously scanning designated areas via 3D sonar downwards-viewing yielding 3D point cloud XYZ file outputs, which are then amalgamated into previously constructed 3D models, ultimately culminating in real-time reconstructions displayed seamlessly via Unity 3D software applications. This is demonstrated visually throughout the figures presented herein (e.g., Figure 24).

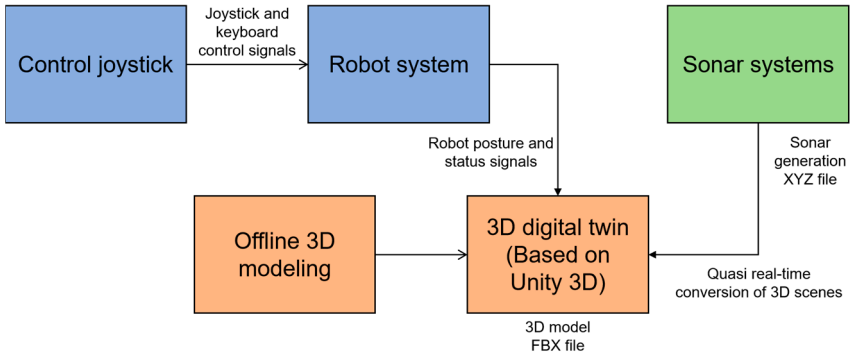

Figure 24. Digital twin system for operation scenarios.

Moreover, the digital twin framework allows for simulation capabilities encompassing operational procedures undertaken by our dredging robots connecting various functional modules together, facilitating training opportunities aimed at enhancing proficiency levels concerning ROV operations [60], as shown in Figure 25. The digital twin scene modeling is depicted in Figure 26, and the scene modeling details are shown in Figure 27.

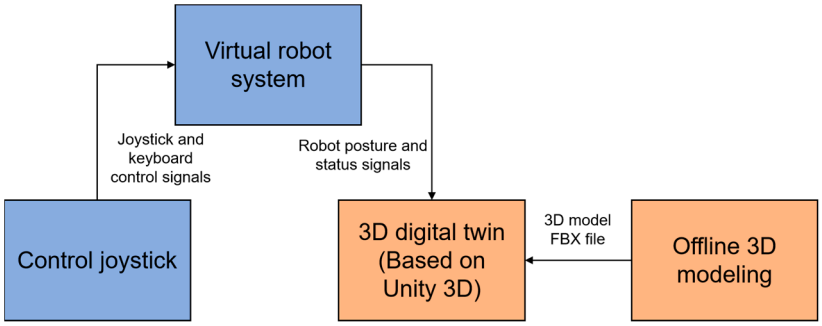

Figure 25. The robot's operation process simulation training system.

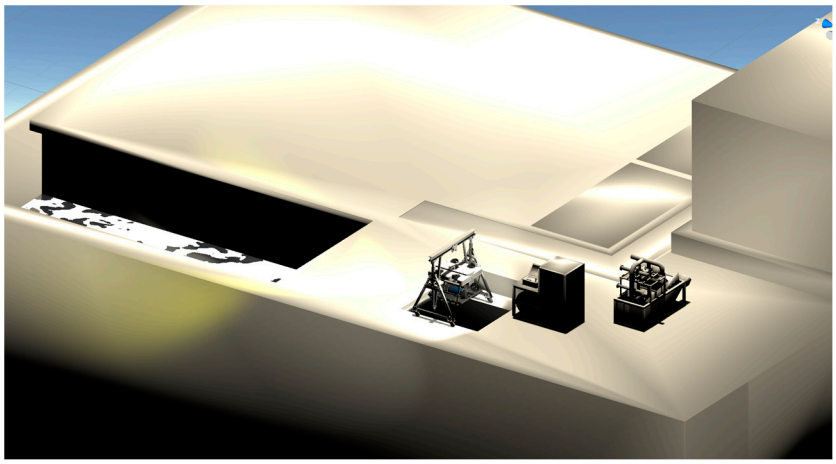

Figure 26. Digital twin scene modeling.

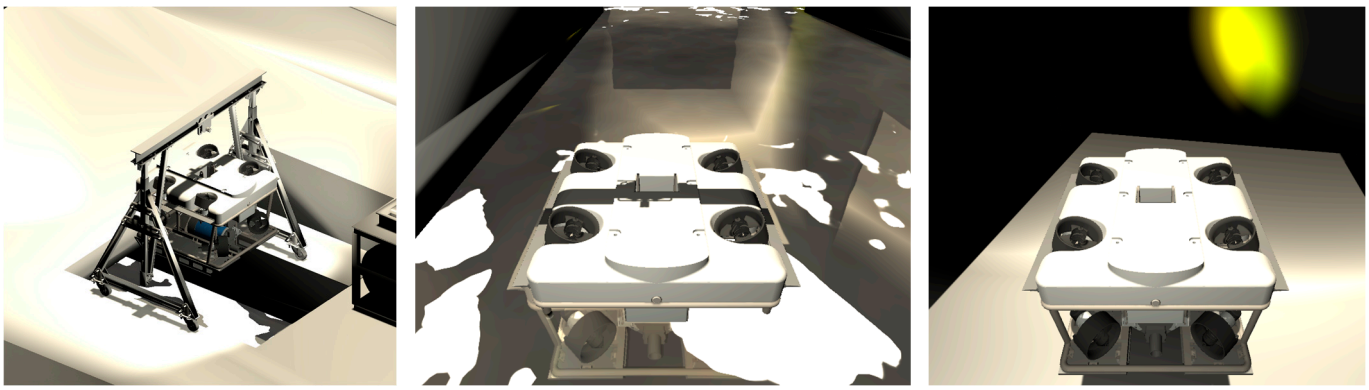

(**a**) (**b**) (**c**)

Figure 27. Scene modeling: (**a**) lifting and launching scenarios of the robot; (**b**) robots entering the water; (**c**) robot underwater operation.

3. Simulation

In the design phase, the 3D structural model of the underwater dredging robot was simultaneously established for simulation and performance optimization.

3.1. Computational Fluid Dynamics Simulation

Computational fluid dynamics (CFD) simulations are performed primarily during the initial design phases, with a focus on optimizing the shapes corresponding to the respective thruster selection/control system development. Additionally, simulations have been carried out to study the effects of underwater jets in dredging operations [61,62].

However, owing to the complexity of the actual operating environment, the above simulations can only verify the feasibility of the underwater dredging robot system. To assess its capabilities accurately, a large amount of experimental data need to be collected and evaluated.

3.1.1. Simulation Analysis

The simulation analysis employs a semi-implicit method for pressure-linked equations (SIMPLE) tailored for pressure-coupled equations. The algorithm operates under two primary assumptions: first, independence between velocity fields and, second, between pressure fields without interdependence, where corrections applied to assumed pressure fields derive from mass conservation constraints associated with computed velocity fields. During velocity correction processes, interactions among correction quantities across different locations are disregarded. Spatial discretization uses a least squares cell-based approach centered on grid calculations whereby physical quantities on grid surfaces necessitate averaging those from adjacent grid centers for accuracy purposes.

At observation points where values stabilize despite increasing computational iterations, convergence behavior in residuals across parameters diminishes progressively until levelling off occurs. Ensuring mass conservation remains paramount alongside considerations for scenarios involving energetic exchanges during computations mandates thorough verification post-calculation steps through the examination of residual curves—for example, demonstrating convergence towards 1×10^{-3}, as illustrated in Figure 28, whereas static pressures appear depicted in Figure 29 alongside the corresponding velocity cloud maps presented in Figure 30.

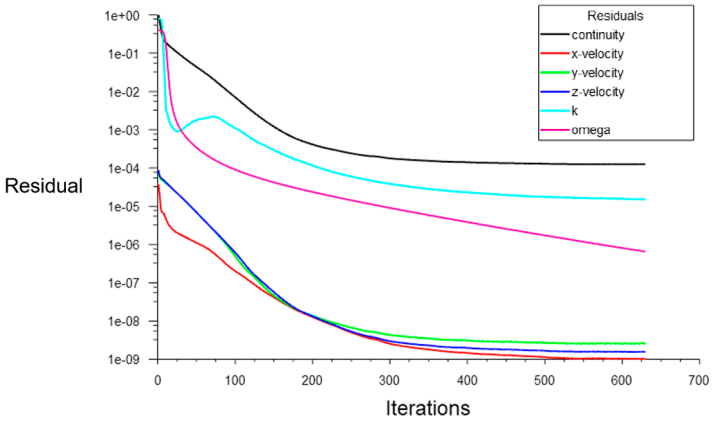

Figure 28. Residual curve.

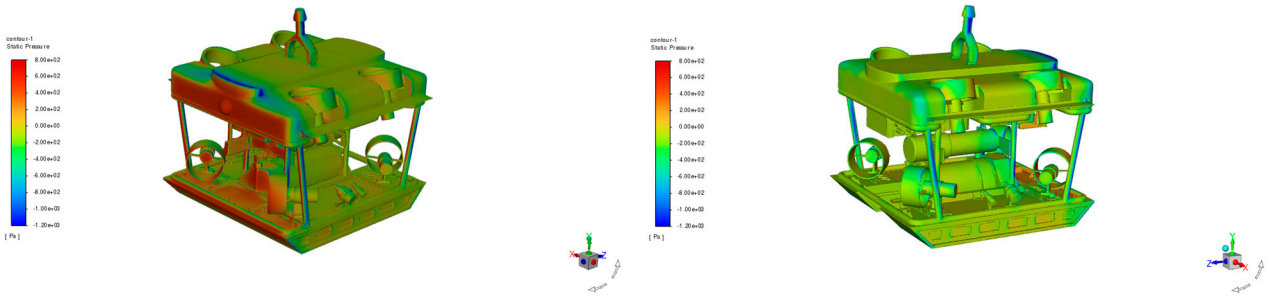

(**a**) (**b**)

Figure 29. Static pressure: (**a**) front; (**b**) side.

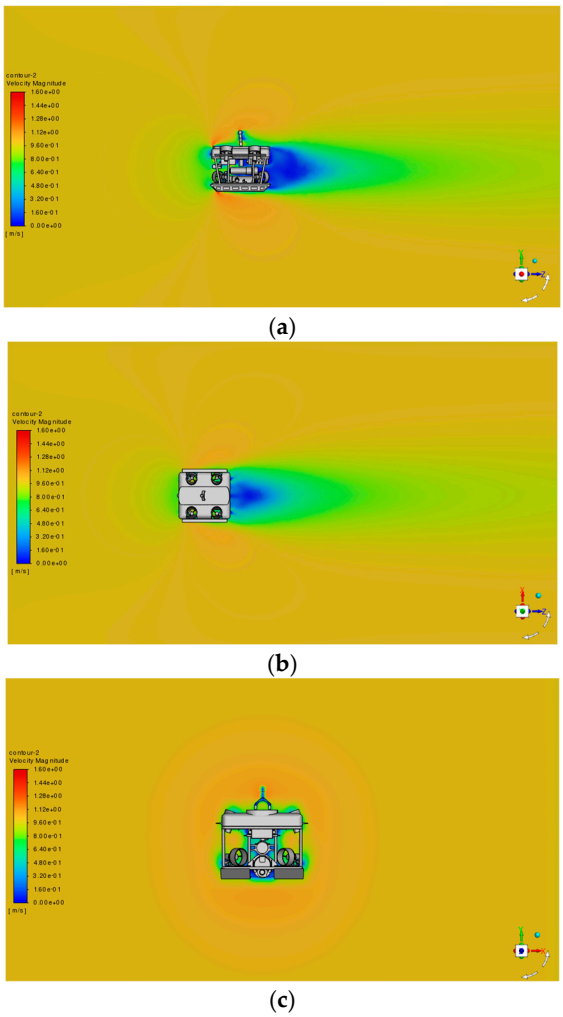

Figure 30. Velocity cloud map: (**a**) on the *yz* section; (**b**) on the *xz* section (horizontal); (**c**) on the *xy* section (perpendicular to the incoming flow).

The subsequent figures illustrate resistance detection curves indicating model resistance measured at 385.1 N when water flows at velocities reaching 1 m/s, as shown in Figure 31.

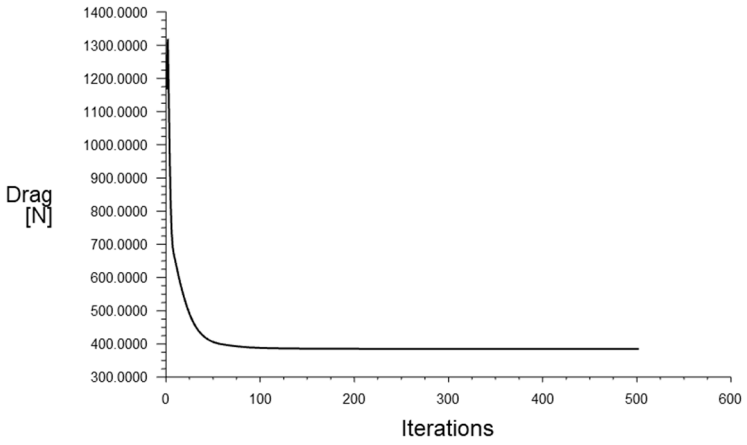

Figure 31. Resistance detection curve.

3.1.2. Particle Analysis

The particle trajectories can provide relevant information on the motion of fluid particles, providing an important reference for the engineering design of fluid mechanics. By analyzing the shape of particle trajectories, various complex motion laws in fluids can be understood.

In the actual dredging process, the heading of ROV is always used as the forward direction and as parallel as possible to the direction of the water flow. The movement of ROV is limited to upward, downward, forward, backward, and left–right translation. According to the distance that the robot moves from the water entry point, the mud pipe is retracted in a timely manner and released to prevent entanglement between the slurry hose and the umbilical cable. Particle simulations depicting robot vertical water movement are represented visually in Figure 32.

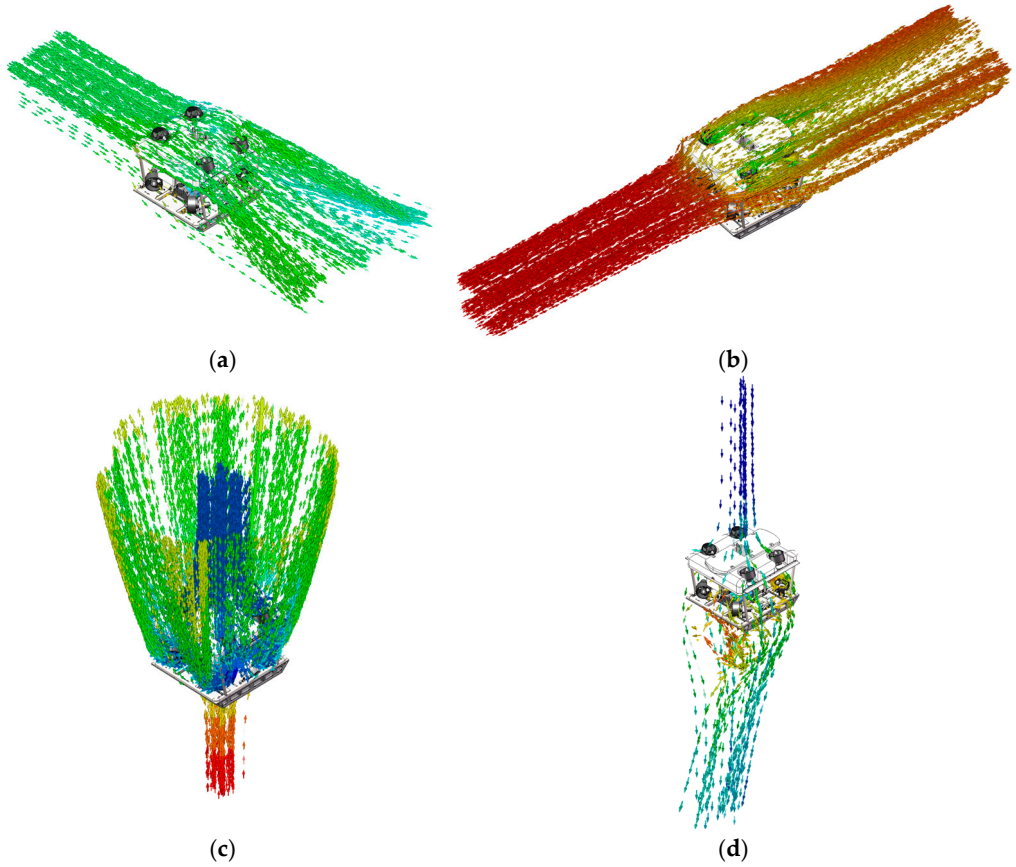

Figure 32. Particle simulation of the robot water flow: (**a**) lateral water flow; (**b**) forwards water flow; (**c**) vertical upwards flow; (**d**) vertical downwards flow.

3.2. ROV Structure Simulation

Structural simulation results are necessary to ensure the structural strength of ROV components during underwater movement and hoisting.

The main frame constitutes an essential load-bearing structural component integral that not only connects various sub-devices but also safeguards them against external forces encountered in underwater environments through collision impact assessments conducted by simulating diverse directional impacts and evaluating strength attributes along deformation responses observed throughout testing phases via stainless steel material selection due to its robust characteristics coupled with its cost-effectiveness, ensuring optimal protection and minimizing losses, thereby enhancing robotic survivability amidst extreme operational conditions. The results derived from these simulations are presented in Figure 33.

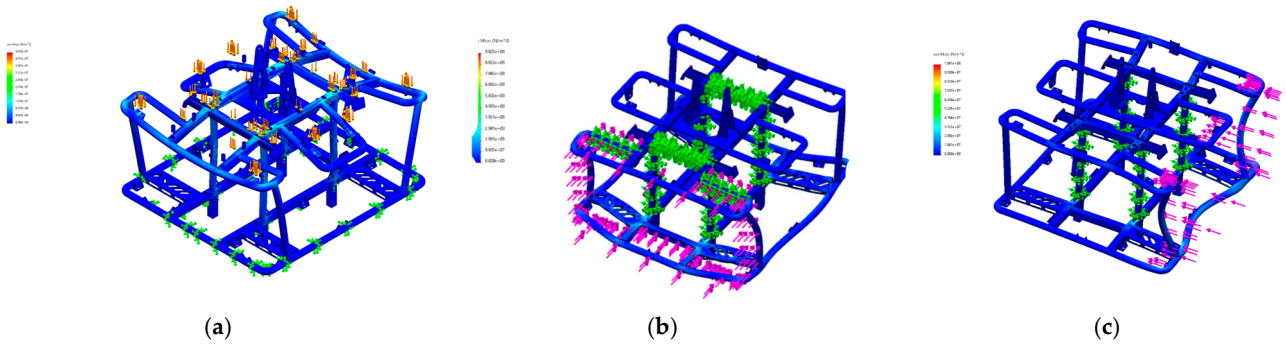

(**a**) (**b**) (**c**)

Figure 33. Analysis of the mechanical characteristics of the robot main frame: (**a**) vertical downwards pressure deformation; (**b**) positive impact yield deformation; (**c**) lateral impact yield deformation.

3.3. Jet Effect Simulation

In the material setup, the fluid is liquid water, and the density of liquid water under standard conditions is $\rho = 1.00 \times 10^3$ kg/m^3.

Further investigations regarding the lifting effects exerted by underwater jets upon sediment situated along bottom substrates were executed, yielding visual representations, as shown in Figure 34:

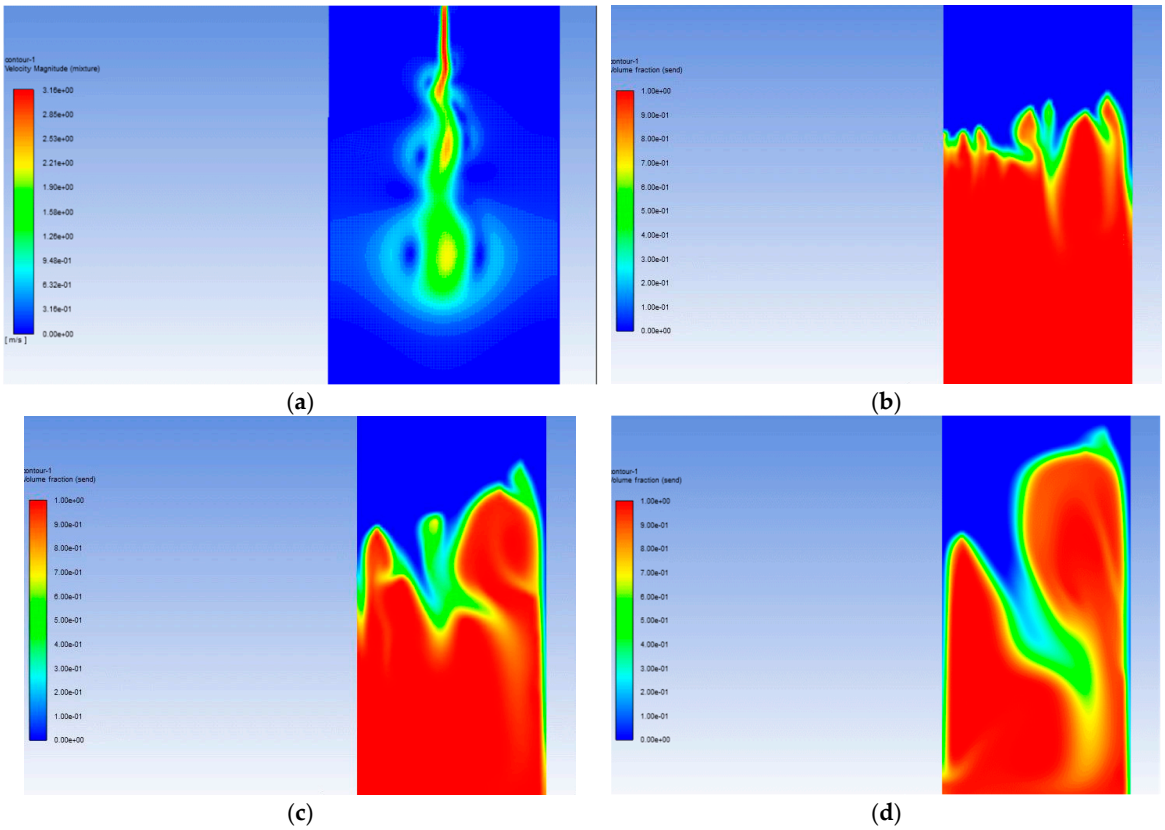

(**a**) (**b**)

(**c**) (**d**)

Figure 34. Underwater jet and effect simulation: (**a**) jet simulation; (**b**) sludge impact effect simulation in the initial moment; (**c**) sludge impact effect simulation in the develop moment; (**d**) sludge impact effect simulation in the spread moment.

At the jet pump flow rate of 4 m^3/h, the distribution of silt and water at various time intervals demonstrates the jet impacts the sediment deposited at the bottom of the water, causing the sediment to disperse outward and reach a state of mixing with water. In

this way, the sediment content at the suction port of the slurry pump can be significantly increased, and the efficiency of dredging can be improved.

4. Test and Results

A series of tests are carried out on the underwater dredging robot in order to verify the key parameters of the proposed robot system and demonstrate its operational capability.

4.1. Experimental Water Tank Testing

Experimental water tank testing was conducted in a small water tank, as illustrated in Figure 35. The experiment was conducted in a clear water environment, with the ROV fully immersed in water to preliminarily test the water tightness performance of each component and the insulation performance of the electrical equipment.

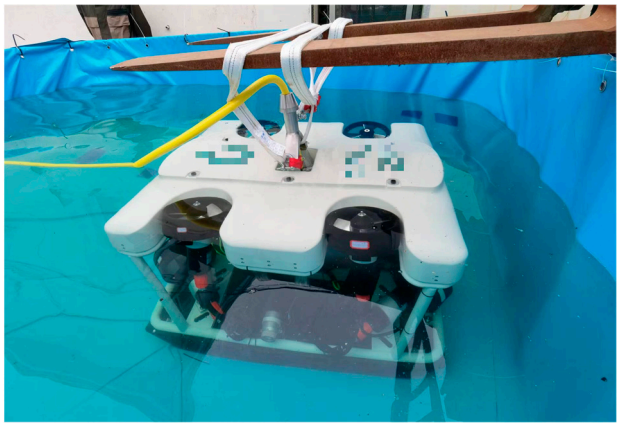

Figure 35. Experimental setup in a small water tank.

4.2. Open Water Area Testing

The open water area testing is located in a static water pool, with a total length of about 50 m, width of 25 m, and depth of 3 m.

The robot is lifted into an open water area for dynamic testing to verify its motion ability when carrying the dredging module. A crane was used to lift the device into the pool, as shown in Figure 36.

The mobility of the underwater dredging robot, equipped with a dredging module, was tested. Subsequently, the slurry hose was connected to the robot, and tests were conducted to assess both the mobility during complete dredging operations and the stability of posture when activating the slurry pump and jet pump. The speed test result of the maximum output power is shown in Table 5.

Table 5. Test of climbing speed.

Sailing Distance	Times (Without Slurry Hose)	Speed (Without Slurry Hose)	Times (with Slurry Hose)	Speed (with Slurry Hose)
50 m	39.65 s	1.26 m/s	127.90 s	0.39 m/s
50 m	37.80 s	1.32 m/s	130.33 s	0.38 m/s
50 m	36.97 s	1.35 m/s	132.56 s	0.38 m/s

The experiment shows that under the PID control of the depth and directional, the robot can always carry out dredging operations in a stable suspended mode and maintain its head pointing at the specified angle.

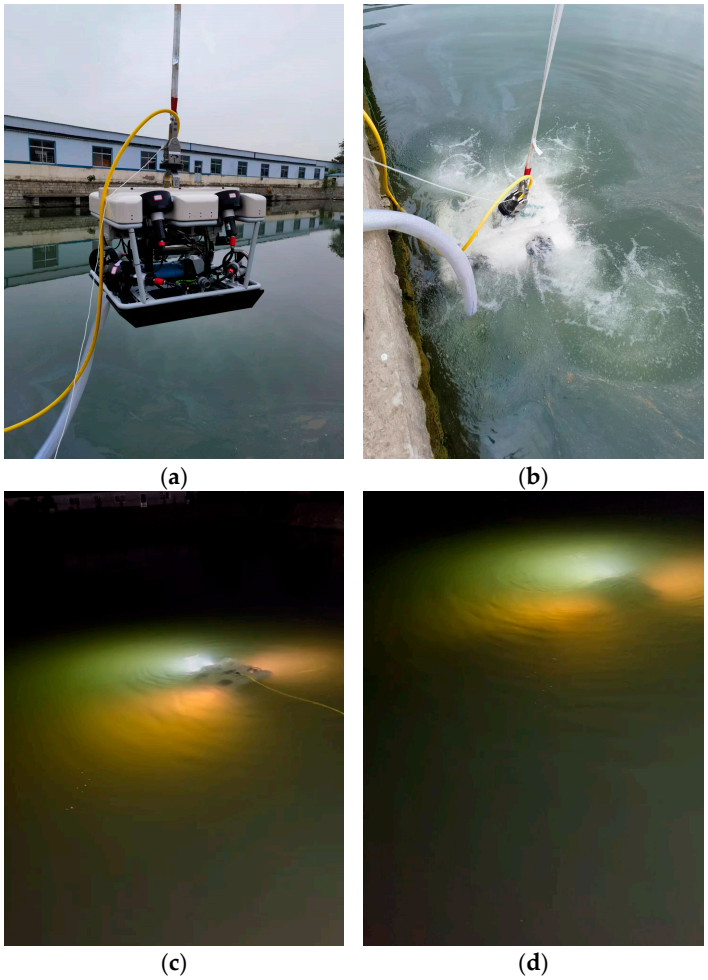

Figure 36. Open water area testing: (**a**) robot lifting into the water; (**b**) vertical thruster action that controls the water entry attitude; (**c**) surface navigation near the water surface; (**d**) suspended in water for fixed-depth navigation.

4.3. Underground Water Treatment Plan Testing

Underwater robots equipped with jet pumps and suction mechanisms conducted underwater sludge sampling experiments in the underground biochemical reaction tank of water treatment plants.

The biochemical reaction tank for the dredging experiment is selected for use in a certain underground water treatment plant. The length of the tank is approximately 44.5 m, and the width is approximately 8.87–9.03 m. The lifting and preparation of the underwater dredging robot are shown in Figure 37.

By adjusting the inflow and outflow of the biochemical reaction tank, the water flow in the tank is kept at a standstill, and the aeration device is temporarily closed to prevent interference with sonar imaging. The robot enters the biochemical reaction tank through a narrow cover plate via a gantry crane, as shown in Figure 38a. When approaching the water surface, the robot turns on the searchlight to indicate its position and assist in bringing the robot back to the ground, as shown in Figure 38b. Owing to the zero visibility underwater, it is necessary to determine the underwater position of the robot through ranging sonar and robot postures; the real-time situation of the control interface is shown in Figure 38c. The color of the extracted slurry can be used to determine the concentration of the solid–liquid mixture and the effectiveness of dredging operations, as shown in Figure 38d.

(**a**) (**b**)

Figure 37. Lifting and preparation of the underwater dredging robot: (**a**)preparation of the dredging operation; (**b**)lifting through cover plate using a gantry crane.

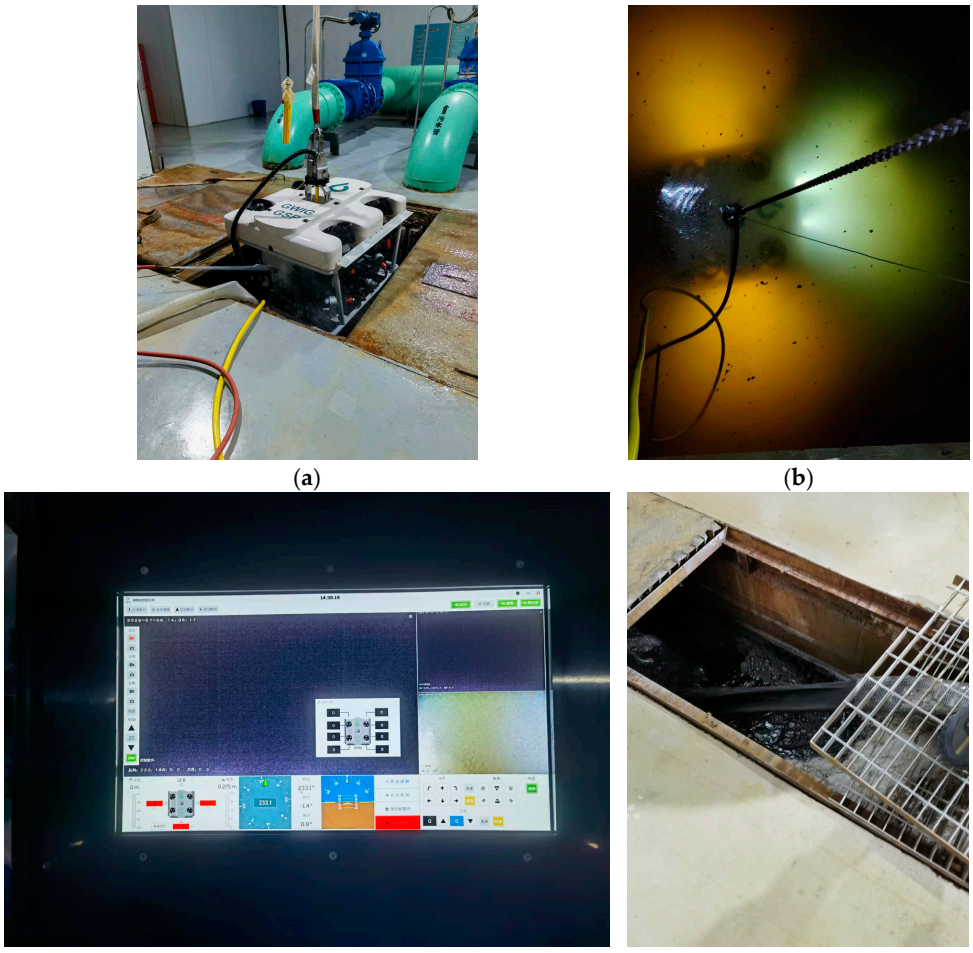

(**a**) (**b**)

(**c**) (**d**)

Figure 38. Actual underwater operation of the robots: (**a**) the robot enters the sewage tank through a narrow cover plate through a gantry crane; (**b**) searchlight for hoisting indication; (**c**) zero-visibility underwater camera image; (**d**) the solid–liquid slurry from the bottom of the biochemical reaction tank is extracted.

After completing underwater operations, the robot removes the buoyancy body and cleans and maintains the main frame and its equipment, as shown in Figure 39.

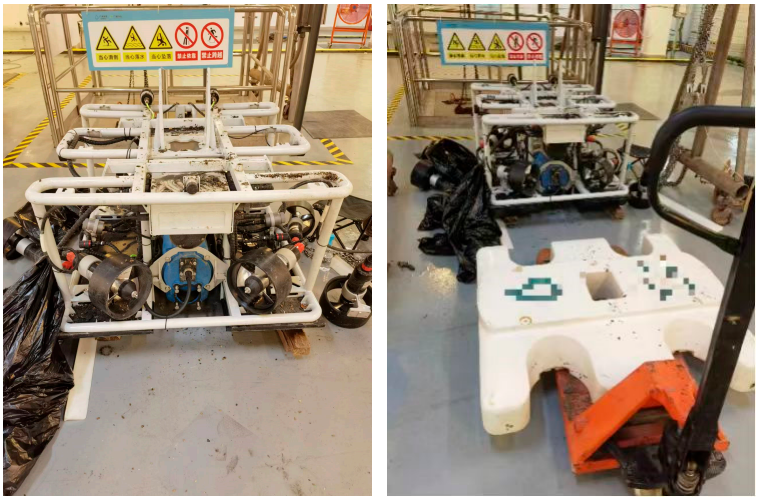

(**a**) (**b**)

Figure 39. Maintenance and cleaning after underwater operation: (**a**) the robot removes the buoyancy body; (**b**) cleaning, handling, and external surface repair of the buoyancy body.

The mud and sand sediment slurry extracted from the biochemical reaction tank needs to undergo solid–liquid separation to concentrate the solid sediment for treatment. The solid–liquid separation effect of the dredging operation is shown in Figure 40a. If space and time are available for natural deposition, the need for solid–liquid separation equipment can be eliminated, and the mud and sand sediments naturally deposited through cofferdams are shown in Figure 40b.

(**a**) (**b**)

Figure 40. The effects of dredging operations: (**a**) solid–liquid separation and (**b**) natural deposition.

4.4. Results and Discussion

Based on historical experience and data measured by downwards-viewing 3D sonar, the average thickness of sediment deposition accumulation is approximately 0.26 m, and the maximum thickness can reach 1.5 m. The calculation of the dredging amount of the biochemical reaction tank is approximately 110 m^3.

The dredging design index of the robot is 25 m^3/h. Compared with previous manual dredging, the efficiency of using the robot is increased by 100%, the labor cost is reduced

by approximately 40%, and the whole process time of a single biochemical reaction tank dredging is controlled within 8 h.

After drying, the mud and sand sediment mentioned above is used as raw material for cement production. A composition analysis was conducted on the dried sludge, as shown in Table 6.

Table 6. Sediment composition analysis of the biochemical reaction tank.

Sample Number	SiO_2	Al_2O_3	Fe_2O_3	CaO	MgO	K_2O	Na_2O	SO_2	Cl	Sum
1	26.65	15.06	6.88	33.94	2.74	1.43	0.23	4.94	0.0540	91.92
2	40.80	22.92	7.73	6.02	1.52	2.42	0.45	0.33	0.0080	82.20

Compared with existing underwater dredging technologies, the robot proposed in this article achieves suspended dredging without touching the underwater bottom facilities [12–18]. Through the above tests, the underwater dredging robot has the following technical features:

1. It can perform motion surveys and operations with six degrees of freedom (including snorkeling, forwards and backwards movement, bow turning, pitch adjustments, etc.).
2. The longitudinal velocity reached the design target of 1.28 m/s (approximately equal to 2.5 knots); the lateral and vertical velocities both reached approximately 1.0 m/s (about 2 knots).
3. The weight in the air does not exceed 300 kg; the ROV can accommodate a variable load capacity of approximately 120 kg while maintaining positive buoyancy equivalent to a maximum of 100 kg through adjustments during actual operations.
4. It can be outfitted with various functional modules tailored for specific tasks (such as dredging, sampling, or surveying).

5. Conclusions

This article presents a novel modular underwater dredging robot specifically designed for underground water treatment plants. The characteristics of the robot, as demonstrated in simulations and tests, make the application of this technology attractive for cost-effective sewage management operations.

Underwater dredging robot operations can be effectively extended to different modes, achieving flexibility and safety in underwater operations. Different underwater dredging modules can be installed, and reasonable counterweights can be achieved based on the mechanical characteristics of each module to achieve the optimal underwater mechanical posture of the robot as a whole.

By installing different buoyancy blocks inside modular skateboards, the overall buoyancy, buoyancy center, and center of gravity of the underwater dredging robot can be adjusted.

The total mass of the basic underwater vehicle, including the operation load, was not more than 300 kg. When the distribution cabinet, umbilical cable, and control panel were added, the complete system weight was less than 500 kg, which can be carried by a small truck.

With the coordination of fixed-point 3D sonar, the system can carry out underwater operations in many narrow water areas. The deployment and retrieval processes require only three to four personnel cooperation, effectively reducing the system's operating costs.

Owing to the highly modular design of robots and the use of electricity as a single power source, system maintenance and repair are also simple enough, providing a flexible approach for underwater operations in sewage environments.

The application of the underwater dredging robot has achieved initial success; the next step is to add more intelligent functions to the robots. Combined with DVL/IMU and fixed-point 3D sonar modeling, the robots could plan the paths in the biochemical reaction tank autonomously, reduce human intervention, and achieve intelligent dredging effects.

With the expansion of offshore and shallow water engineering projects, there is an increasing demand for comprehensive underwater environment monitoring, terrain surveys of rivers and lakes, the detection of underwater mechanisms in water conservancy and hydro power facilities, aquaculture operations, and other related tasks. This necessitates the development of a cost-effective and versatile underwater robot capable of adjusting its operational parameters based on varying requirements within constrained underwater environments and accommodating different operational modules for specific tasks [63–65].

The robots described in this article can be applied in the above areas. In addition to dredging operations in underground water treatment plants, the robots have broad prospects in the water, environmental protection, aquaculture, energy, and mining industries.

Author Contributions: Conceptualization, X.D. and J.L.; methodology, J.L.; software, J.L.; validation, X.D., J.L. and C.P.; formal analysis, J.L.; investigation, J.L.; resources, J.L.; data curation, J.L.; writing—original draft preparation, J.L.; writing—review and editing, X.D.; visualization, C.P.; supervision, X.D.; project administration, J.L.; funding acquisition, J.L. and C.P. All authors have read and agreed to the published version of the manuscript.

Funding: This research was funded by the Zhuhai Social Development Science and Technology Plan Project (2320004000154).

Data Availability Statement: The raw data supporting the conclusions of this article will be made available by the authors on request.

Conflicts of Interest: The authors declare no conflict of interest.

References

1. Ma, N.; Xu, Y. Water Environmental Risks Encountered during Urbanization in Valley Areas and the Potential Mitigation Effects of Utilizing Reclaimed Water. *Sustainability* **2024**, *16*, 7573. [CrossRef]
2. Lu, Y.; An, H.; Li, C.; Liu, C. Environmental Impact Analysis and Carbon Emission Reduction Pathways by Upgrading Wastewater Treatment Plant: A Case Study of Upgrading Project at a Wastewater Treatment Plant in Dongguan, China. *Water* **2024**, *16*, 596. [CrossRef]
3. Jover-Smet, M.; Martín-Pascual, J.; Trapote, A. Model of Suspended Solids Removal in the Primary Sedimentation Tanks for the Treatment of Urban Wastewater. *Water* **2017**, *9*, 448. [CrossRef]
4. Mukwevho, N.; Ntsasa, N.; Mkhohlakali, A.; Mabowa, M.H.; Chimuka, L.; Tshilongo, J.; Letsoalo, M.R. The Impact of Induced Industrial and Urban Toxic Elements on Sediment Quality. *Water* **2024**, *16*, 2485. [CrossRef]
5. Zhang, D.; Li, H.; Li, X.; Ao, D.; Wang, N. Source of Methanogens and Characteristics of Methane Emission in Two Wastewater Treatment Plants in Xi'an. *Water* **2024**, *16*, 2101. [CrossRef]
6. Ding, H.H.; Kotova, P.; Shaw, C.; Hong, Y.; Chang, S. Impacts of Temperature and Solids Retention Time, and Possible Mechanisms of Biological Hydrolysis Pretreatment on Anaerobic Digestion. *Water* **2020**, *12*, 3166. [CrossRef]
7. Purzycki, M.; Komorowska, A.; Ilnicka, A.; Papiez, J.; Szymanska, E. From ROVs to AUVs—Optimization and Analysis of Underwater Vehicles Design. In Proceedings of the 2022 45th Jubilee International Convention on Information, Communication and Electronic Technology (MIPRO), Opatija, Croatia, 23–27 May 2022; IEEE: Opatija, Croatia, 2022; pp. 1517–1521.
8. Gómez-Bravo, F.; Garrocho-Cruz, A.; Marín-Cañas, O.; Pulido-Calvo, I.; Gutierrez-Estrada, J.C.; Peregrín-Rubio, A. A Control Architecture for Developing Reactive Hybrid Remotely Operated Underwater Vehicles. *Machines* **2023**, *12*, 1. [CrossRef]
9. Wood, S.; Harris, W.; Ismail, T.; Malone, J.-M.; Nanney, M.; Ojeda, J.; Pugatch, B.; Vandedrinck, S. Hybrid Robot Crawler/Flyer for Use in Underwater Archaeology. In Proceedings of the 2013 OCEANS, San Diego, CA, USA, 23–27 September 2013; pp. 1–11.
10. Xue, Y.; Wang, S.; Ma, W.; Zeng, Z. Underwater Wall-Climbing Inspection ROV Scheme Design and Flow Resistance Simulation Based on BlueROV2 Modification. In Proceedings of the 2023 IEEE 3rd International Conference on Software Engineering and Artificial Intelligence (SEAI), Xiamen, China, 16–18 June 2023; pp. 215–219.
11. Mai, C.; Pedersen, S.; Hansen, L.; Jepsen, K.L.; Yang, Z. Subsea Infrastructure Inspection: A Review Study. In Proceedings of the 2016 IEEE International Conference on Underwater System Technology: Theory and Applications (USYS), Penang, Malaysia, 13–14 December 2016; IEEE: Penang, Malaysia, 2016; pp. 71–76.
12. Li, X.; Wen, H.; Cao, J.; Yao, B.; Lian, L.; Mao, Z. Adaptive Sliding Mode Controller Combined with Pseudo-Inverse-Based Thruster Allocator Design for ROV with Variable Coefficients. *Ocean Eng.* **2023**, *286*, 115530. [CrossRef]
13. Li, Y.; He, D.; Ma, F.; Liu, P.; Liu, Y. MPC-Based Trajectory Tracking Control of Unmanned Underwater Tracked Bulldozer Considering Track Slipping and Motion Smoothing. *Ocean Eng.* **2023**, *279*, 114449. [CrossRef]
14. Li, X.; Wen, H.; Fu, J.; Zhang, X.; Zhou, H.; Yao, B.; Lian, L.; Yu, D.; Mao, L. Modeling and System Analysis of Floating Underwater Vehicle with Variable Mass and Center of Gravity. *Ocean Eng.* **2023**, *267*, 113303. [CrossRef]

15. Zhang, X.; Li, X.; Fu, J.; Yao, B.; Lian, L.; Hu, Y. Design, Simulation and Experimental Research on an Underwater Dredging Robot. In Proceedings of the OCEANS 2024, Singapore, 15–18 April 2024; IEEE: Singapore, 2024; pp. 1–7.
16. Arykantsev, V.; Kalinin, Y.; Chernyshev, V. Determination of the Underwater Walking Robotic Mini Dredger Loading Capacity by the Finite Element Modeling. In Proceedings of the 2023 2nd International Conference on Machine Learning, Control, and Robotics (MLCR), Nanjing, China, 9–11 December 2023; IEEE: Nanjing, China, 2023; pp. 125–130.
17. Li, T.J.; Wu, M.-H.; Feng, Y.-n.; Zhou, W. Analysis of Desilting Efficiency of Spiral Dredging Auger Based on EDEM. In Proceedings of the 2024 8th International Conference on Robotics, Control and Automation (ICRCA), Shanghai, China, 12–14 January 2024; IEEE: Shanghai, China, 2024; pp. 366–369.
18. Shademani, S.; Zarafshan, P.; Khashechi, M.; Kianmehr, M.H.; Hashemy, S.M. Design and Analysis of a Dredger Robot for Covered Irrigation Canals. In Proceedings of the 2017 5th RSI International Conference on Robotics and Mechatronics (ICRoM), Tehran, Iran, 25–27 October 2017; IEEE: Tehran, Iran, 2017; pp. 162–167.
19. Yang, C.; Liu, S.; Su, H.; Zhang, L.; Xia, Q.; Chen, Y. Review of Underwater Adsorptive-Operating Robots: Design and Application. *Ocean Eng.* **2024**, *294*, 116794. [CrossRef]
20. Ji, L.; He, X.; Li, W.; Tian, F.; Shi, W.; Zhou, L.; Liu, Z.; Yang, Y.; Xiao, C.; Agarwal, R. Research Progress of Advanced Design Method, Numerical Simulation, and Experimental Technology of Pumps in Deep-Sea Resource Exploitation. *Water* **2024**, *16*, 1881. [CrossRef]
21. Wang, Y.; Han, C.; Zhao, X. Optimization Study on Sequential Emptying and Dredging for Water Diversity Reservoir Group. *Water* **2024**, *16*, 2482. [CrossRef]
22. Wang, T.; Wang, Z.; Zhang, B. Mechanism Design and Experiment of a Bionic Turtle Dredging Robot. *Machines* **2021**, *9*, 86. [CrossRef]
23. Wang, L.; Kang, Y.; Wang, Y.; Zhao, Z.; Shang, L.; Song, X.; Xu, D.; Cheng, R. Optimization Design of a Winch Suction Underwater Dredging Robot Using Orthogonal Experimental Design. *J. Mar. Sci. Eng.* **2024**, *12*, 741. [CrossRef]
24. Shiosawa, T.; Takagi, K.; Inoue, T. Experimental and Theoretical Study on the Motion of ROV with Crawler System. In Proceedings of the OCEANS 2010 MTS/IEEE SEATTLE, Seattle, WA, USA, 20–23 September 2010; IEEE: Seattle, WA, USA, 2010; pp. 1–5.
25. Inoue, T.; Katsui, T.; Tahara, J.; Itoh, K.; Yoshida, H.; Ishibashi, S.; Takagi, K. Experimental Research on Movability Characteristic of Crawler Driven ROV. In Proceedings of the OCEANS 2008, Quebec City, QC, Canada, 15–18 September 2008; IEEE: Quebec City, QC, Canada, 2008; pp. 1–6.
26. Nakayama, K.; Saito, A. Practical Marine TDEM Systems Using ROV for the Ocean Bottom Hydrothermal Deposits. In Proceedings of the 2016 Techno-Ocean (Techno-Ocean), Kobe, Japan, 6–8 October 2016; IEEE: Kobe, Japan, 2016; pp. 643–647.
27. Utada, H.; Baba, K.; Shimizu, H.; Shiobara, H.; Tada, N. Ocean Bottom Measurements of the Earth's Electric Field Using Long Cable Installed by ROV. In Proceedings of the 2013 IEEE International Underwater Technology Symposium (UT), Tokyo, Japan, 5–8 March 2013; IEEE: Tokyo, Japan, 2013; pp. 1–6.
28. Akram, W.; Casavola, A.; Kapetanović, N.; Miškovic, N. A Visual Servoing Scheme for Autonomous Aquaculture Net Pens Inspection Using ROV. *Sensors* **2022**, *22*, 3525. [CrossRef] [PubMed]
29. Chen, J.; Xin, Y.; Zhang, Y.; Li, J.; Yang, W.; Li, Z. A Novel Deep-Sea Exploration Equipment: Combined Multisite Lander and Rover ROV System. In Proceedings of the OCEANS 2021: San Diego—Porto, San Diego, CA, USA, 20–23 September 2021; IEEE: San Diego, CA, USA, 2021; pp. 1–5.
30. Joochim, C.; Phadungthin, R.; Srikitsuwan, S. Design and Development of a Remotely Operated Underwater Vehicle. In Proceedings of the 2015 16th International Conference on Research and Education in Mechatronics (REM), Bochum, Germany, 18–20 November 2015; IEEE: Bochum, Germany, 2015; pp. 148–153.
31. Rentzow, E.; Muller, T.; Golz, M.; Ritz, S.; Kurowski, M.; Jeinsch, T. Modeling and Control of a Highly Modular Underwater Vehicle with Experimental Results. In Proceedings of the 2021 European Control Conference (ECC), Delft, The Netherlands, 29 June–2 July 2021; IEEE: Delft, The Netherlands, 2021; pp. 2245–2250.
32. Song, Y.S.; Arshad, M.R. Thruster Modeling for a Hovering Autonomous Underwater Vehicle Considering Thruster-Thruster and Thruster-Hull Interaction. In Proceedings of the 2016 IEEE International Conference on Underwater System Technology: Theory and Applications (USYS), Penang, Malaysia, 13–14 December 2016; IEEE: Penang, Malaysia, 2016; pp. 100–104.
33. Healey, A.J.; Rock, S.M.; Cody, S.; Miles, D.; Brown, J.P. Toward an Improved Understanding of Thruster Dynamics for Underwater Vehicles. *IEEE J. Ocean. Eng.* **1995**, *20*, 354–361. [CrossRef]
34. Zhang, M.; Liu, W.; Wang, Y.; Liu, X. Weak Thruster Fault Prediction Method for Autonomous Underwater Vehicle. In Proceedings of the OCEANS 2016, Shanghai, China, 10–13 April 2016; IEEE: Shanghai, China, 2016; pp. 1–5.
35. Gavrilina, E.; Veltishev, V.; Kropotov, A. Attitude Control System of a Highly Maneuverable Hybrid ROV for Ship-Hull Inspection. In Proceedings of the OCEANS 2021: San Diego—Porto, San Diego, CA, USA, 20–23 September 2021; IEEE: San Diego, CA, USA, 2021; pp. 1–6.
36. Cao, J.; Liu, C.; Yao, B.; Lian, L. Simulation and Stability Analysis of the 200-Meter ROV in the Absence of One Thruster. In Proceedings of the 2013 OCEANS, San Diego, CA, USA, 23–27 September 2013; pp. 1–6.
37. Hao, L.-Y.; Yu, Y.; Li, T.-S.; Li, H. Quantized Output-Feedback Control for Unmanned Marine Vehicles With Thruster Faults via Sliding-Mode Technique. *IEEE Trans. Cybern.* **2022**, *52*, 9363–9376. [CrossRef] [PubMed]

38. Wang, Y.; Zhang, M.; Chu, Z.; Liu, X. Fault-Tolerant Control Based on Adaptive Sliding Mode for Underwater Vehicle with Thruster Fault. In Proceedings of the 11th World Congress on Intelligent Control and Automation, Shenyang, China, 29 June–4 July 2014; IEEE: Shenyang, China, 2014; pp. 5323–5328.
39. Binugroho, E.H.; Sanggar Dewanto, R.; Pramadihanto, D. eROV: Preliminary Design of 5 DOF ROV Using 6 Thrusters Configuration. In Proceedings of the 2018 International Electronics Symposium on Engineering Technology and Applications (IES-ETA), Bali, Indonesia, 29–30 October 2018; IEEE: Bali, Indonesia, 2018; pp. 281–287.
40. Dukan, F. ROV Motion Control Systems. Ph.D. Dissertation, Norwegian University of Science and Technology, Trondheim, Norway, 2014.
41. Salem, K.M.; Rady, M.; Aly, H.; Elshimy, H. Design and Implementation of a Six-Degrees-of-Freedom Underwater Remotely Operated Vehicle. *Appl. Sci.* **2023**, *13*, 6870. [CrossRef]
42. Zhang, D.; Wang, X.; Zhao, M.; Hong, L.; Li, X. Numerical Investigation on Hydrodynamic Characteristics and Drag Influence of an Open-Frame Remotely Operated Underwater Vehicle. *J. Mar. Sci. Eng.* **2023**, *11*, 2143. [CrossRef]
43. Rethfeldt, C.; Lack, S.; Jeinsch, T. Optimization-Based Actuator Allocation for Underwater Vehicles with Variable Buoyancy Systems. In Proceedings of the 2023 International Interdisciplinary PhD Workshop (IIPhDW), Wismar, Germany, 3–5 May 2023; IEEE: Wismar, Germany, 2023; pp. 1–6.
44. Tangirala, S.; Dzielski, J. A Variable Buoyancy Control System for a Large AUV. *IEEE J. Oceanic Eng.* **2007**, *32*, 762–771. [CrossRef]
45. Khalid, M.U.; Ahsan, M.; Kamal, O.; Najeeb, U. Modeling and Trajectory Tracking of Remotely Operated Underwater Vehicle Using Higher Order Sliding Mode Control. In Proceedings of the 2019 16th International Bhurban Conference on Applied Sciences and Technology (IBCAST), Islamabad, Pakistan, 8–12 January 2019; IEEE: Islamabad, Pakistan, 2019; pp. 855–860.
46. Moody, R. The Design, Construction, and Testing of a Flexible Fin Propelled Autonomous Underwater Vehicle. In Proceedings of the MTS/IEEE Oceans 2001—An Ocean Odyssey, Honolulu, HI, USA, 5–8 November 2001; Conference Proceedings (IEEE Cat. No. 01CH37295). Marine Technol. Soc: Honolulu, HI, USA, 2001; Volume 4, pp. 2703–2707.
47. Kocak, D.M.; Neely, J.W.; Holt, J.; Miyake, M. A Specialized ROV for Cleaning Groundwater Recharge Basins. In Proceedings of the Oceans '99. MTS/IEEE Riding the Crest into the 21st Century Conference and Exhibition, Seattle, WA, USA, 13–16 September1 1999; Conference Proceedings (IEEE Cat. No. 99CH37008). IEEE & Marine Technol. Soc: Seattle, WA, USA, 1999; Volume 2, pp. 567–579.
48. Makavita, C.D.; Jayasinghe, S.G.; Nguyen, H.D.; Ranmuthugala, D. Experimental Study of Command Governor Adaptive Control for Unmanned Underwater Vehicles. *IEEE Trans. Contr. Syst. Technol.* **2019**, *27*, 332–345. [CrossRef]
49. Bingul, Z.; Gul, K. Intelligent-PID with PD Feedforward Trajectory Tracking Control of an Autonomous Underwater Vehicle. *Machines* **2023**, *11*, 300. [CrossRef]
50. Kang, H.; Cho, G.R.; Lee, M.-J.; Ki, G.; Kim, M.-G.; Li, J.-H. Power Distribution for Motion Control of URI-T, Underwater Cable Burying ROV. In Proceedings of the OCEANS 2019, Marseille, France, 17–20 June 2019; IEEE: Marseille, France, 2019; pp. 1–4.
51. Rezk, H.; Abdalla, O.; Tolba, M.A.; Zaky, M.M. Optimum Size of Battery-Less Energy Sources Autonomous Hybrid Power System for Water Pumping Applications. In Proceedings of the 2020 International Youth Conference on Radio Electronics, Electrical and Power Engineering (REEPE), Moscow, Russia, 12–14 March 2020; IEEE: Moscow, Russia, 2020; pp. 1–6.
52. Qian, H.; Liu, J.; Xu, M.; Fan, C.; Duan, Z. Experimental Investigation on the Impact of Sand Particle Size on the Jet Pump Wall Surface Erosion. *J. Mar. Sci. Eng.* **2024**, *12*, 1390. [CrossRef]
53. Wang, X.; Wu, Y.; Jia, P.; Liu, H.; Yun, F.; Li, Z.; Wang, L. Orthogonal Experimental Design Based Nozzle Geometry Optimization for the Underwater Abrasive Water Jet. *Machines* **2022**, *10*, 1243. [CrossRef]
54. Pellegrini, M.; Saccani, C.; Guzzini, A. Environmental Life Cycle Assessment of Innovative Ejectors Plant Technology for Sediment By-Pass in Harbours and Ports. *Sustainability* **2024**, *16*, 7809. [CrossRef]
55. Dong, H.; Wang, D.; Li, Z.; Zhang, Q.; Li, Y.; Zhang, J.; Zhang, L.; Zhang, L. Experimental Study on Infiltration of Seawater Bentonite Slurry. *Buildings* **2024**, *14*, 2609. [CrossRef]
56. Guo, X.S.; Nian, T.K.; Wang, Z.T.; Zhao, W.; Fan, N.; Jiao, H.B. Low-Temperature Rheological Behavior of Submarine Mudflows. *J. Waterw. Port Coast. Ocean Eng.* **2019**, *146*, 04019043. [CrossRef]
57. Guo, X.S.; Nian, T.K.; Gu, Z.D.; Li, D.Y.; Fan, N.; Zheng, D.F. Evaluation Methodology of Laminar-Turbulent Flow State for Fluidized Material with Special Reference to Submarine Landslide. *J. Waterw. Port Coast. Ocean Eng.* **2021**, *147*, 04020048. [CrossRef]
58. Pyo, J.; Yu, S.-C. Development of AUV (MI) for Strong Ocean Current and Zero-Visibility Condition. In Proceedings of the 2016 IEEE/OES Autonomous Underwater Vehicles (AUV), Tokyo, Japan, 6–9 November 2016; IEEE: Tokyo, Japan, 2016; pp. 54–57.
59. Wang, F.; Yang, Y.; Zhou, J.; Zhang, W. An Onboard Point Cloud Semantic Segmentation System for Robotic Platforms. *Machines* **2023**, *11*, 571. [CrossRef]
60. Mendonca, R.; Santana, P.; Marques, F.; Lourenco, A.; Silva, J.; Barata, J. Kelpie: A ROS-Based Multi-Robot Simulator for Water Surface and Aerial Vehicles. In Proceedings of the 2013 IEEE International Conference on Systems, Man, and Cybernetics, Manchester, UK, 13–16 October 2013; IEEE: Manchester, UK, 2013; pp. 3645–3650.
61. Yoon, H.K.; Nguyen, T.T.; Van Nguyen, M. Establishment of Equations of Motion of a ROV Using CFD Technique. In Proceedings of the OCEANS 2017, Anchorage, AK, USA, 18–21 September 2017; pp. 1–6.

62. Sahili, J.; Hamoud, A.E.-H.; Jammoul, A. ROV Design Optimization: Effect on Stability and Drag Force. In Proceedings of the 2018 6th RSI International Conference on Robotics and Mechatronics (IcRoM), Tehran, Iran, 23–25 October 2018; IEEE: Tehran, Iran, 2018; pp. 413–417.
63. Osen, O.L.; Sandvik, R.-I.; Berge Trygstad, J.; Rogne, V.; Zhang, H. A Novel Low Cost ROV for Aquaculture Application. In Proceedings of the OCEANS 2017, Anchorage, AK, USA, 18–21 September 2017; pp. 1–7.
64. Wright, N.G. SeaDrone a Low Cost Dual Drone/ROV Technology That Can Cross the Sea Boundary. In Proceedings of the OCEANS 2017, Anchorage, AK, USA, 18–21 September 2017; pp. 1–4.
65. Cufí, X.; El-Fakdi, A.; Medina, A. A Low Cost Educational ROV Platform for Promoting Engineering among Young Students: ROV R2B2, New Challenges. In Proceedings of the OCEANS 2023, Limerick, Ireland, 5–8 June 2023; IEEE: Limerick, Ireland, 2023; pp. 1–7.